

Soft X-ray emission from warm gas in IllustrisTNG circum–cluster environments

I – Sample Properties, Methods and Initial Results

Celine Gouin^{1*}, Massimiliano Bonamente², Daniela Galárraga-Espinosa³, Stephen Walker²,
Mohammad Mirakhor²

¹ Université Paris-Saclay, CNRS, Institut d’Astrophysique Spatiale, 91405, Orsay, France

² University of Alabama in Huntsville, Department of Physics and Astronomy, Huntsville, AL 35899

³ Max-Planck Institute for Astrophysics, Karl-Schwarzschild-Str. 1, D-85741 Garching, Germany

June 9, 2023

ABSTRACT

Context. Whereas X-ray clusters are extensively used for cosmology, their idealistic modelling, through the hypotheses of spherical symmetry and hydrostatic equilibrium, are more and more being questioned. Along these lines, the soft X-ray emission detected in tens of clusters with ROSAT was found to be higher than what expected from the idealistic hot gas modelling, pointing to our incomplete understanding of these objects.

Aims. Given that cluster environments are at the interface between the hot intra–cluster medium (ICM), warm circumgalactic medium (WCGM) and warm–hot intergalactic medium (WHIM), we aim to explore the relative soft X-ray emission of different gas phases in circum–cluster environments.

Method. By using the most massive halos in IllustrisTNG at $z = 0$, we have predicted the hydrodynamical properties of the gas from cluster centers to their outskirts ($5 R_{200}$), and modelled their X–ray radiation for various plasma phases.

Results. First, we found that the radial profile of temperature, density, metallicity and clumpiness of the ICM are in good agreement with recent X-ray observations of clusters. Secondly, we have developed a method to predict the radial profile of soft X-ray emission in different bands, the column density of ions and the X–ray absorption lines (O VIII, O VII, Ne IX, and Ne IX) of warm-hot gas inside and around clusters.

Conclusion. The warm gas (in the form of both WCGM and WHIM gas) is a strong emitter in soft X-ray bands, and is qualitatively consistent with the observational measurements. Our results suggest that the cluster *soft excess* is induced by the thermal emission of warm gas in the circum–cluster environments.

Key words. Galaxies: cluster: general – large-scale structure of Universe – Methods: statistical – Methods: numerical – X-ray – WHIM

1. Introduction: X–rays from circum–cluster environments and the missing baryons problem

X–ray emission from galaxy clusters is used extensively to probe a variety of astrophysical phenomena and to study cosmology. Since the early surveys of the X–ray sky (Giacconi et al. 1972), it became apparent that clusters are powerful sources of X–ray emission, originating primarily from a hot phase ($\geq 10^7$ K) of the intergalactic medium that is kept bound by a massive dark matter halo that significantly outweighs visible galaxies (e.g. Bahcall & Sarazin 1977). The X–ray emission is primarily thermal in origin, with free–free bremsstrahlung providing the bulk of the emissivity, with the presence of emission lines from such elements as iron that are not fully ionized (e.g. Mitchell et al. 1976; Serlemitsos et al. 1977).

Among some of the key uses of X–ray emission from galaxy clusters are the determination of cosmological parameters that describe dark matter and dark energy (e.g. Allen et al. 2004; Vikhlinin et al. 2009; Mantz et al. 2014,

2022) and the Hubble constant (e.g. Bonamente et al. 2006; Wan et al. 2021), the understanding of the growth of cosmic structure on the largest scales (see Walker et al. 2019, for recent review), and the study of the complex feedback mechanism between the cluster’s galaxies and their active galactic nuclei (e.g. Yang & Reynolds 2016). At the heart of all these studies is the interpretation of the detected emission as radiation from a hot intra–cluster medium (ICM) that is in approximate hydrostatic equilibrium with its underlying matter potential.

At soft X–ray wavelengths, broadly defined as photon energies substantially below the peak of the X–ray emission from the hot ICM (≤ 1 keV) and above the effective cut–off imposed by Galactic absorption (~ 0.1 keV), X-ray emission from and near clusters is less well studied. This is due to a combination of the lower effective energy and poorer calibration of most X–ray missions (e.g. Nevalainen et al. 2010) towards lower photon energies, the effects of Galactic foregrounds (e.g. Snowden et al. 1995) that are both time– and space–variables, and the contamination from sub–virial phases.

* E-mail: celine.gouin@ias.u-psud.fr

Numerical simulations provide the means to study the thermodynamics of the gas in and near cluster environments. With the advanced of baryonic physics models through sub-grid and particle techniques, the current generation of large hydrodynamical simulations, such as IllustrisTNG (Nelson et al. 2019), HorizonAGN (Dubois et al. 2016), Magneticum (Hirschmann et al. 2014; Dolag et al. 2016; Ragagnin et al. 2017) and TheThreeHundred project (Cui et al. 2018), provides statistical sample of highly resolved simulated clusters to deeply investigate their gas properties, and in particular their thermal footprint for X-Ray interpretation. Probing the gas physics through state-of-the-art simulations have already revealed departure to hydrostatic equilibrium inside clusters (e.g. Gianfagna et al. 2023), resulting of turbulence and bulk motion (e.g. Angelinelli et al. 2020), and proposed correction for this bias in X-ray (Ansarifard et al. 2020). More generally, numerous investigations have been recently done to probe the ICM physics by using numerical simulations, such as their chemical enrichment (Biffi et al. 2018), and their thermal and pressure profiles for accurately predict scaling relations (e.g. Barnes et al. 2017; Pop et al. 2022) to better interpret X-ray emission of clusters.

For our cluster gas investigation, we are using the TNG300-1 simulation, the larger box of IllustrisTNG simulations ($\sim 300 \text{ Mpc}^3$) with the highest spatial resolution, to take advantage of both, a statistical sample of clusters, and an accurate modeling of the baryonic physics (Pillepich et al. 2018). Using TNG300-1 simulation, Martizzi et al. (2019a) and Galárraga-Espinosa et al. (2021) have highlighted that hot gas is dominant inside clusters, as the knots of the large-scale cosmic web, whereas warm diffuse gas can be used to trace filamentary structures at $z = 0$. Such improvement in our understanding of cluster and cosmic gas has recently allow to forecast on warm and hot gas observations through OVII and OVIII emission lines for the next generation spectrometers (Paribelli et al. 2022; Butler Contreras et al. 2023; Tuominen et al. 2023). Focusing exclusively on cluster environments, Gouin et al. (2022) have explored the gas thermodynamics in TNG300-1, showing that clusters are the interface between two dominated gas phases: the warm and the hot gas. The warm gas in filaments infalls to the connected clusters, undergoes motions of accretion and ejection at cluster borders, and transitions then into the hot gas phase, inside clusters.

This project aims to fill the gap in our theoretical and observational understanding of soft X-ray emission in and near galaxy clusters, using the Gouin et al. (2022) IllustrisTNG sample of massive clusters studied out to $5 \times r_{200}$. We refer to these astrophysical volumes as the *circum-cluster environment* (as introduced by Yoon & Putman 2013), i.e, the region in and surrounding galaxy clusters, including the transition between the inner virialized ICM and the outer accreting sub-virial plasmas that is expected to contain the highest-density WHIM. The main motivation for this study of the soft X-ray emission near clusters is the expectation that a significant fraction of the universe’s baryons at the present epoch is in a warm-hot intergalactic medium (WHIM) at $\log T(\text{K}) \leq 7$ (e.g. Cen & Ostriker 1999; Davé et al. 2001). These baryons are widely expected to bridge the *missing baryons* gap, i.e., resolve the observational discrepancy between the lower amount of low- z baryons compared to high- z baryons (e.g. Danforth et al. 2016). Although evidence is mounting that WHIM

filaments are responsible for both emission (e.g. Tanimura et al. 2020; Mirakhor et al. 2022; Tanimura et al. 2022) and absorption of X-rays (e.g. Kovács et al. 2019; Spence et al. 2023) in amounts that are consistent with the missing fraction of baryons, the regions near clusters where filaments are expected to be densest remain relatively unexplored, in part because of the difficulties on disentangling the contributions from the virial and sub-virial phases. One exception is the detection of the cluster *soft excess* emission in a number of clusters with ROSAT (e.g. Bonamente et al. 2003, 2022) and other soft X-ray instruments, which is consistent with the detection of WHIM filaments projecting onto massive clusters. One of the main motivations of this project is therefore to address the contribution to the projected X-ray emission at soft X-ray energies from hot and sub-virial phases in and around massive clusters, and other aspects of cluster physics that are related to this X-ray emission.

This paper, which is intended to be the first of a series, describes the methods of analysis of the IllustrisTNG data to obtain averaged radial profiles of thermodynamic quantities of interest for the prediction of the X-ray emission, via density, temperature, chemical abundances, volume covering fraction and clumpiness of the gas phases, and initial results on the projection of the emissivity from the different gas phases in and around clusters. This paper is structured as follows: Sect. 2 presents the IllustrisTNG simulations and their analysis to obtain radial profiles; Sect. 3 describes our analytical method to project radial profiles on a detector plane, Sect. 4 describes the methods to obtain projected profiles of radiated power and X-ray surface brightness that can be compared with observations, and preliminary results from that analysis. Sect. 5 presents a brief discussion and our conclusions. Subsequent papers will make use of these methods for a more in-depth analysis of the emission from sub-virial gas in and around clusters, its astrophysical and cosmological implications, and related aspects of cluster physics.

2. Thermodynamical profiles from IllustrisTNG circum-cluster environments: Methods and comparison with observations

2.1. Cluster selection from IllustrisTNG simulation

Starting from the halo catalog of the TNG300-1 simulation at $z = 0$, we select all friends-of-friends halos (FoF) with masses $M_{200} > 10^{14} M_{\odot}/h$. In this catalog, the radial scale of FoF halos R_{200} is defined as the radius of a sphere which encloses a mass M_{200} with an average density equal to 200 times the critical density of the Universe. From our mass selection of 153 clusters, we consider only the 138 clusters whose centers are more distant than $5 \times R_{200}$ from the simulation box edges, to fully explore cluster environments. The main properties of the IllustrisTNG cluster sample are reported in Table 1. In this table, we define also the three mass bins, considering in the following analysis, the low-mass clusters M_1 (with $M_{200} \in 10^{[14.0-14.1]} M_{\odot}/h$), the middle cluster mass range M_2 (with $M_{200} \in 10^{[14.1-14.5]} M_{\odot}/h$), and the most massive clusters M_3 with $M_{200} > 10^{14.5} M_{\odot}/h$.

Sample	Mass Range	$\langle M_{200} \rangle$	$\langle R_{200} \rangle$	Number of clusters
All clusters	$\log(M_{200}[M_{\odot}/h]) > 14$	$1.97 \times 10^{14} M_{\odot}/h$	$0.92/h$ Mpc	138
M_1	$14.0 < \log(M_{200}[M_{\odot}/h]) < 14.1$	$1.13 \times 10^{14} M_{\odot}/h$	$0.78/h$ Mpc	47
M_2	$14.1 < \log(M_{200}[M_{\odot}/h]) < 14.5$	$1.91 \times 10^{14} M_{\odot}/h$	$0.92/h$ Mpc	78
M_3	$\log(M_{200}[M_{\odot}/h]) > 14.5$	$5.37 \times 10^{14} M_{\odot}/h$	$1.3/h$ Mpc	13

Table 1. Main properties of the all cluster sample, and its three mass bins M_1 , M_2 and M_3 .

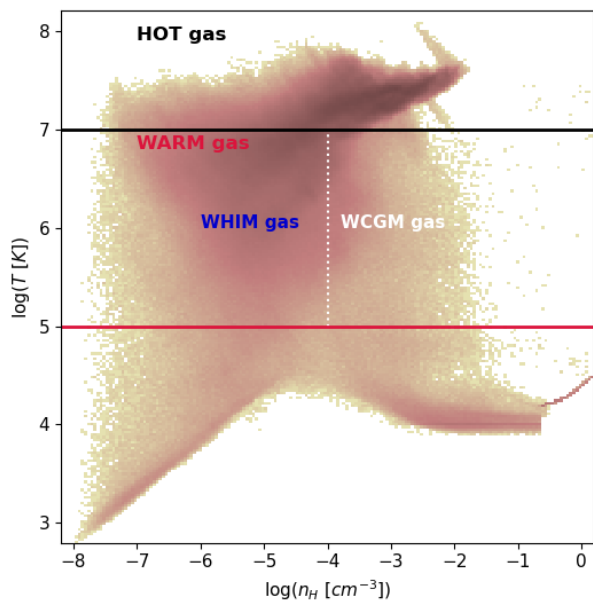


Fig. 1. Phase-space of the gas cells around a given cluster in the TNG300-1 simulation, shown by the normalised 2D histogram. The hot gas is defined with a temperature $T[\text{K}] > 10^7$, and the WARM gas with temperature between $10^5 < T[\text{K}] < 10^7$. The WHIM gas is a sub-sample of the WARM gas, with the condition to be diffuse, i.e., its density is $n_H[\text{cm}^{-3}] < 10^{-4}$.

2.2. Gas phases

The gas cells are separated depending of their temperature and density, in order to distinguish different gas phases. We have followed the temperature and density cuts of [Martizzi et al. \(2019a\)](#), commonly used in hydrodynamical simulation analyses to explore gas phase transitions (see e.g. [Galárraga-Espinosa et al. 2021](#)). As demonstrated by [Gouin et al. \(2022\)](#), cluster environments are dominated by two main phases, mostly the Hot ICM ($T[\text{K}] > 10^7$) inside the clusters, and the warm diffuse gas phase (WHIM: $10^5 < T[\text{K}] < 10^7$ and $n_H[\text{cm}^{-3}] < 10^{-4}$) outside clusters (see Fig. 1 and 2 of [Gouin et al. 2022](#)). In this study, we defined also the WARM gas as all gas cells with warm temperature $10^5 < T[\text{K}] < 10^7$, thus accounting of both WHIM and WCGM gas phase ($10^5 < T[\text{K}] < 10^7$ and $n_H[\text{cm}^{-3}] > 10^{-4}$). We illustrated this different gas phase definitions in the phase-space diagram Fig. 1. Although the distinction between WHIM and WCGM is used as a simple means to identify the lower- and higher-density portions of the WARM sub-virial phase.

In Fig. 2, we show the spatial distribution of these different gas phases for a given cluster environment (up to $5 R_{200}$). As expected from [Gouin et al. \(2022\)](#), the hot gas phase is tracing the gas distribution inside clusters, whereas

WHIM gas is representing the filamentary patterns around cluster (see also [Planelles et al. 2018](#)). Interestingly, our extended definition of WARM gas, show the WHIM gas with the addition of warm clumps gas. Indeed, by plotting only WCGM gas in Fig. 2, one can see that small dense clumps of gas are resulting from WCGM phase. As expected by [Martizzi et al. \(2019a\)](#), this definition of WCGM and WHIM gases therefore represents physically different gas phases.

2.3. Numerical computation of radial thermodynamic profiles

For each thermodynamic quantity of the gas, we average the value by considering the gas cells (labeled by the index i and with a volume V_i) inside radial shells (labeled by the index k , with r_k normalized by R_{200}) around the cluster center. The average of a quantity Q is given by:

$$Q(r_k) = \frac{\sum_{i \in R_k} Q_i \times V_i}{\sum_{i \in R_k} V_i} \quad (1)$$

with the $k = 1, \dots, 50$ index labelling the 50 logarithmically-spaced radial distances around the center, ranging from 0 to $5 R_{200}$, and the radial range is $R_k = [r_{k-1}, r_k]$. The averages according to (1) therefore represent the volume-weighted average value of the quantity for a given gas phase (either all gas cells, HOT, WHIM, or WARM gas). These averages are shown as solid lines in Figures 3, 6 and 7 for, respectively, the electron n_e and hydrogen density n_H , the temperature T , and the metal abundance Z .

The average profiles according to Eq. (1), however, do not take into account the *volume covering fraction* of a given phase (hot ICM, WHIM and WARM), defined as

$$f_k = \frac{\sum_{i \in R_k} V_i}{V_{\text{shell},k}}, \quad (2)$$

where $V_{\text{shell},k}$ is the usual volume of a spherical shell between radii r_{k-1} and r_k . The volume covering fractions are shown in Fig. 4, where the covering fraction is approximately 100% for the HOT phase near the cluster center, while it is significantly less than unity for the other phases, and it changes with radius for all phases. Indeed, the volume covering fraction of a given gas phase is intrinsically related to its abundance. Therefore, it follows the same radial trend than the relative abundance of different gas phases discussed in [Gouin et al. \(2022\)](#), with two dominant phases in circum-cluster environments: the HOT gas phase (up to $\sim 1 R_{200}$) and the WARM gas phase at larger radial distances.

In order to predict the X-ray emission of different gas phases, it is also useful to determine the radial profiles of

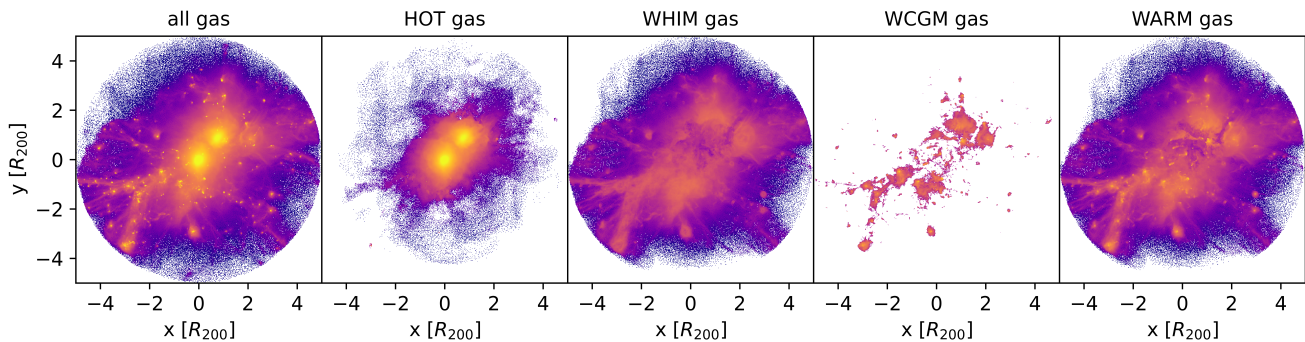


Fig. 2. Distribution of gas within $5 R_{200}$ around a given massive cluster. The first panel shows the distribution of all the gas cells, the second one only the HOT gas, the third one only the WHIM gas, and the left panel shows the WARM gas.

the mass density, accounting for the volume covered by a given phase. This is obtained via

$$\rho_k = \frac{\sum_{i \in R_k} m_i}{V_{\text{shell},k}}, \quad (3)$$

where m_i is the mass contained in the i -th gas cell that is included in the radial bin R_k . In Eq. (3), the density is in units of $(M_{\odot}/h) \cdot (\text{Mpc}/h)^{-3}$, and it includes all the gas (*i.e.* electrons, hydrogen and all other ions). These mass density profiles are shown as dashed lines in Fig. 3, after a normalization that results in the conversion to units of equivalent H atoms cm^{-3} , to match the units of the electron and hydrogen density in the same figure. One can first notice that, when taking into account the volume fraction of a given gas phase, the radial profile of the phase drastically changes. For example, we see that the WARM gas is denser than the ICM inside clusters (the solid red line is higher than the black one), which can be explained by the fact that colder gas can more easily collapse and become denser. However, given that WARM gas is extremely rare compared to the ICM gas phase inside clusters (see in Fig. 4 and as illustrated in Fig. 2), its mass density (weighted by volume fraction, dashed lines) is much lower than the ICM. For a given phase, the difference between solid and dashed density curves in Fig. 3 is therefore simply explained by the different radial dependencies of the volume covering fractions.

All of these thermodynamic profiles have been computed for each simulated cluster, and then averaged for all the clusters, and for the three different cluster mass bins. The detail on the averaging procedure over the cluster population has been detailed in appendix A where we also discuss the difference between mean and median averages. Indeed, individual clumps in some circum-cluster environments can artificially boost the mean thermodynamic profiles. In appendix B, we have also reported in the tables B.1 and B.2, the values of density, volume fraction, temperature, metal abundance of the different gas phases in and around the clusters averaged over all, M_1 , M_2 and M_3 clusters.

2.4. Radial thermodynamic profiles - Comparisons to observations

The hot ICM mass density is compared with selected recent observations in Fig. 5, namely the Ghirardini et al. (2019)

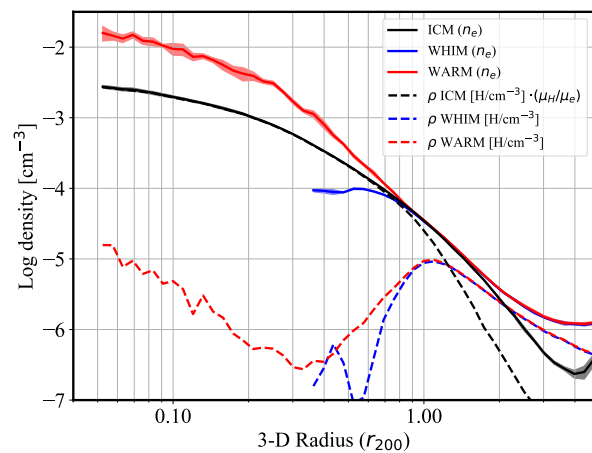


Fig. 3. Right panel : The electron density n_e calculated according to the averaging of Eq. 1 is the solid line, and the mass density calculated according to the averaging of Eq. 3 is in dashed line. We show the median profile over all the cluster sample.

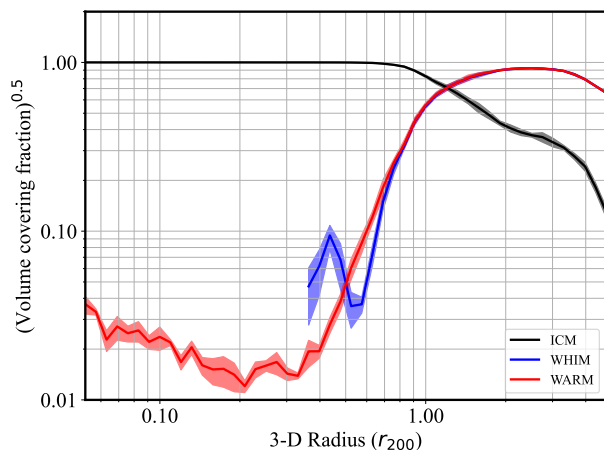


Fig. 4. Volume covering fractions, same sample as in Fig. 3.

analysis of the X-COP sample of 12 massive clusters, the Eckert et al. (2012) results of a sample of 31 nearby clusters, and the detailed analysis of the Coma cluster by Mirakhor & Walker (2020), all covering a radial range approximately equal to at least r_{200} . The IllustrisTNG profile of the av-

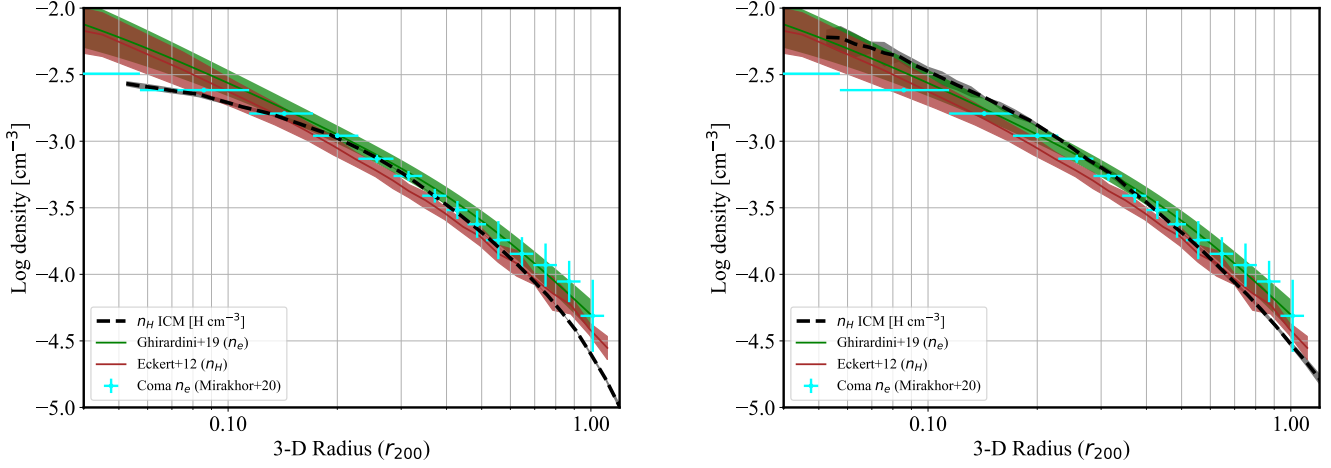


Fig. 5. Zoom-in of Fig. 3, the median radial profiles of the mass density for the ICM gas phase for all the clusters (left panel), and the most massive ones (M_3 mass bin, right panel). We highlight the comparison with X-COP observations (Eckert et al. 2012; Ghirardini et al. 2019) and Coma cluster (Mirakhor & Walker 2020).

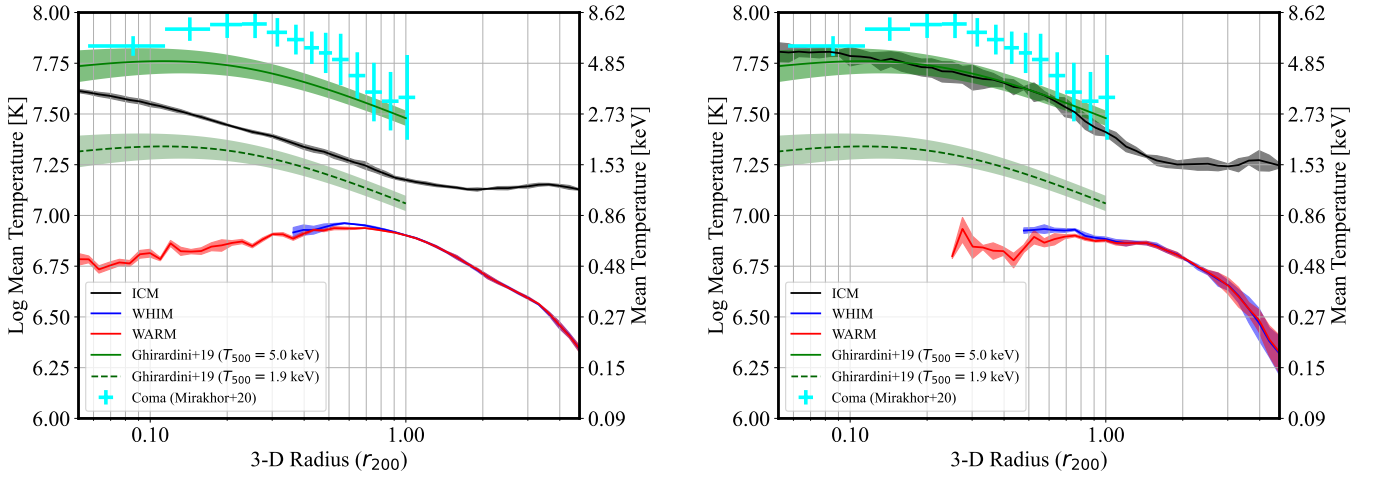


Fig. 6. Radial profiles of temperatures, same samples as in Fig. 5.

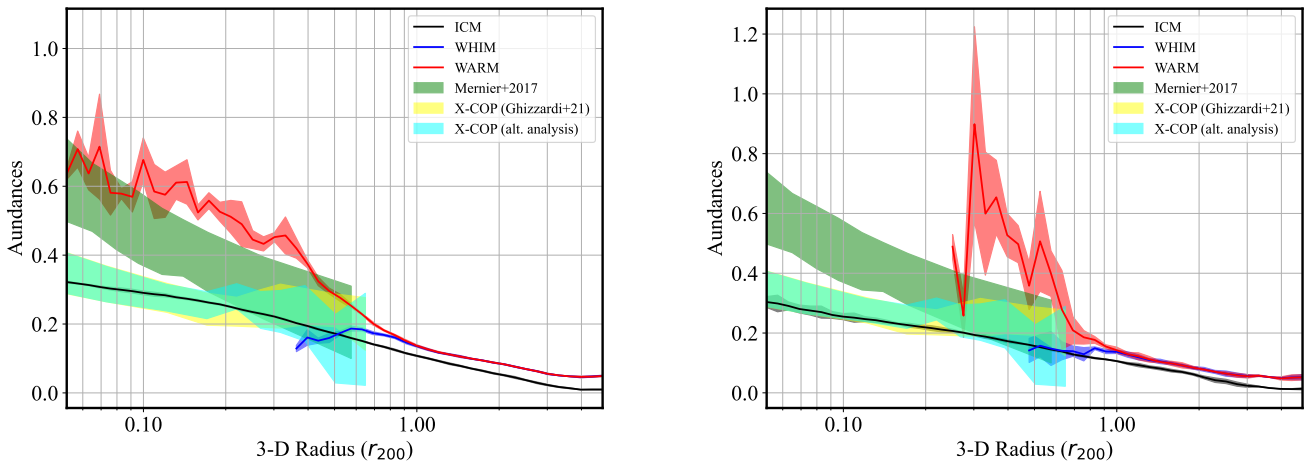


Fig. 7. Radial profiles of abundances, same samples as in Fig. 5.

average ICM n_H density (dashed line in Fig. 5) is in excellent agreement with the observational results, especially for the most massive cluster sample M_3 whose masses are most directly comparable to those of the Ghirardini et al. (2019), Eckert et al. (2012) and Mirakhor & Walker (2020) observations.

The radial profiles of the mean temperature are shown in Fig. 6, along with a comparison with the observational results from Ghirardini et al. (2019) and Mirakhor & Walker (2020). The Ghirardini et al. (2019) temperature profiles are scaled according to the temperature at r_{500} (T_{500}), and therefore Fig. 6 shows two observational constraints corresponding to two values of T_{500} that correspond approximately to the most massive sample and to the least massive sample. The radial profile of the hot ICM temperature for the M_3 sample is in perfect agreement with the Ghirardini et al. (2019) constraints for $T_{500} = 5$ keV. The Coma radial profile has a slightly higher temperature, given that its mass of $M_{200} = 8.550 \pm 0.55 M_\odot$ corresponds to one of the largest in our IllustrisTNG sample.

The average metal abundance profiles are shown in Fig. 7. The metal abundance of the ICM is in excellent agreement with the Ghizzardi et al. (2021) constraints at all radii. Mernier et al. (2017), on the other hand, finds a significantly higher metal abundance at lower radii, progressively reaching the $A \simeq 0.2$ Solar value towards the virial radius, in agreement with the IllustrisTNG profiles. This higher metallicity inside clusters might be induced by WARM gas phase, as it is suggested by our predictions according to Fig. 7.

2.5. Clumpiness of the gas

Inhomogeneities in the gas have a direct impact on several physical quantities derived from observations of galaxy clusters and the warm-hot phases. As is explained in detail in Sect. 4 below, the measured X-ray surface brightness is proportional to the square of the density. Therefore, it is the average $\langle n_e^2 \rangle$, and not $\langle n_e \rangle$, that is the primary observable in X-rays. In turn, this means that inferences on such fundamental quantities as the gas mass and the total mass as inferred by hydrostatic equilibrium, both function of n_e , rely on an estimate of the linear density and therefore on an assessment of inhomogeneities in the plasma (for a review, see e.g. Walker et al. 2019).

Following Nagai & Lau (2011), we use the following averages of the electron density,

$$\left\{ \begin{aligned} \langle n_e(r_k) \rangle &= \frac{\sum_{i \in R_k} n_{e_i} \times V_i}{\sum_{i \in R_k} V_i} \\ \langle n_e^2(r_k) \rangle &= \frac{\sum_{i \in R_k} n_{e_i}^2 \times V_i}{\sum_{i \in R_k} V_i} \end{aligned} \right. \quad (4)$$

to define the *clumping factor* as

$$C(r_k) = \frac{\langle n_e^2(r_k) \rangle}{\langle n_e(r_k) \rangle^2} \geq 1. \quad (5)$$

A value of the clumping factor greater than one indicates gas that is not uniformly distributed over the respective spherical shell of provenance, but rather with regions

of significantly higher or lower (including null) density, contributing to a variance in the distribution of the densities that results in $\langle n_e^2(r_k) \rangle > \langle n_e(r_k) \rangle^2$. In Appendix B, the table B.3 also reports the values of \sqrt{C} for selected radii, for the three gas phases and for the 3 mass bins.

Figure 8 shows the median radial profile of the clumping factor average over all the clusters, and for different gas phases. Considering the full gas distribution (purple line), the clumpiness of the gas is very low inside clusters and becomes significantly clumpy beyond the virial radius, while the density of the hot ICM is quite uniform within r_{200} . However, the WARM gas clumpiness (red line) is higher inside clusters, as suggested previously in the illustration Fig. A.1. Therefore, we conclude that the WARM gas phase is colder, with larger metallicity and more clumpy than the ICM in circum-cluster environments. In contrast, WHIM gas only is by definition more diffuse, and thus with a lower clumping factor than WARM gas. Interestingly, we found also that all gas phases follow the same radial trend with low clumpiness inside clusters, and rapidly increasing beyond the virial radius.

The measurements of the clumping factor of Nagai & Lau (2011), using the simulations of Kravtsov (1999); Kravtsov et al. (2002), shows an increasing radial trend that reaches a value of $C \simeq 10$ at $2 \times R_{200}$, somewhat higher than our results yet qualitatively consistent with an increasing importance of clumpiness at larger distances from the cluster's center. This radial evolution of clumpiness is also consistent with previous numerical investigations (see e.g. Roncarelli et al. 2013; Ansarifard et al. 2020). More recently, Angelinelli et al. (2021) has performed a similar analysis with the Itasca simulations (see Fig. 5 in their paper), resulting in quantitatively similar results that indicate an increasing radial trend of the clumpiness with radius reaching an approximate value of $\sqrt{C} \simeq 3$ at $5 \times r_{500} \simeq 3 \times r_{200}$ (their definition of the clumpiness factor includes the square-root operation). An interesting point is to consider either mean or median averaging of clumping factor, a point discussed in Appendix A, showing that median is less sensitive to individual gas inhomogeneities in the full cluster sample (see also Towler et al. 2023, reaching a similar conclusion). Finally, Planelles et al. (2017) have revealed that the inclusion of AGN feedback in simulations is helping the ICM to be more homogeneous, reducing the clumping factor values, and found similar clumpiness radial trend, with a slightly higher value of $\sqrt{C} = 1.2$ at r_{200} .

Observationally, it is challenging to measure the gas clumping directly, primarily due to the limited spatial resolution of the X-ray instruments and the small angular size of most distant clusters. Morandi et al. (2017) was able to estimate a clumping factor of $C \sim 2-3$ at r_{200} for the lower-mass galaxy group NGC 2563, again in agreement with the IllustrisTNG predictions, although for a system of lower mass than the clusters in our sample. For the nearby Virgo cluster, Mirakhor & Walker (2021) measured a small value of the clumping factor ($C \simeq 1.1$) at small radii from the center ($r \ll r_{200}$) from X-ray observations, again in quantitative agreement with our measurements. Moreover, Eckert et al. (2015b) used a sample of 31 clusters ($z = 0.04 - 0.2$) observed by ROSAT to measure the clumping factor at the level of $\sqrt{C} \leq 1.1$ within r_{500} , and to set constraints of the order $\sqrt{C} \leq 1.5 - 2$ beyond that radius.

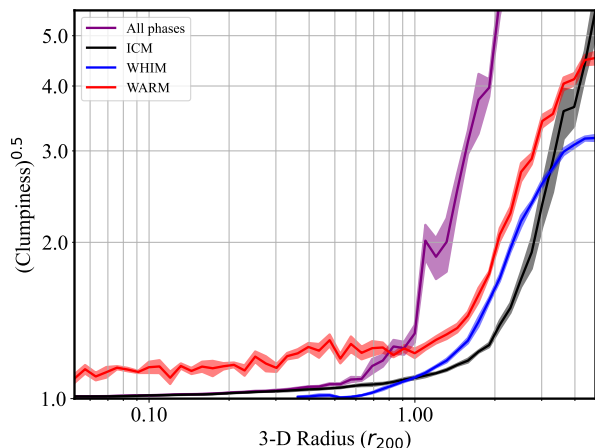


Fig. 8. Median radial profiles of the clumping factor average over all the clusters.

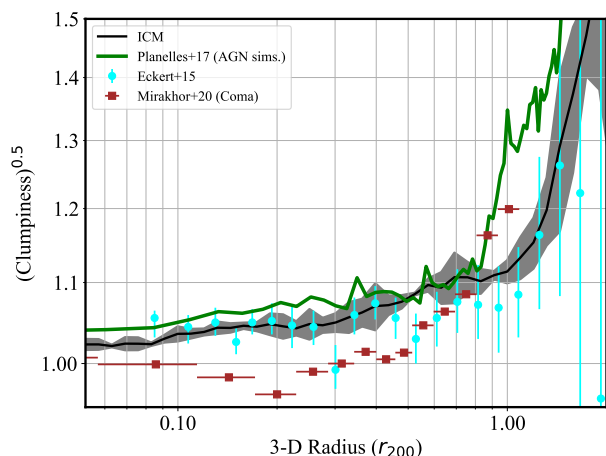


Fig. 9. Comparison of the ICM clumpiness factor for the most massive cluster (M_3 mass bin) with the simulations of Planelles et al. (2017) in a sample of clusters in a comparable mass range, the clumpiness in Coma from Mirakhor & Walker (2020) and the Eckert et al. (2015a) measurements.

In Fig. 9, we compare our ICM clumpiness radial profile of most massive clusters with previous AGN simulation from Planelles et al. (2017), and the observational measurements from Eckert et al. (2015b) and Mirakhor & Walker (2021). Inside clusters ($< 1 R_{200}$), a good agreement is found with both previous numerical predictions and recent observations. Interestingly, at larger radii ($> 1 R_{200}$), Planelles et al. (2017) show somewhat lower clumping factor than our prediction, although with the same increasing radial trend as our profile. This difference can be due to different AGN modeling, which accurately reproduces observed statistical trends at $z = 0$ in IllustrisTNG (Pillepich et al. 2018; Nelson et al. 2019). The accurate AGN feedback modeling in IllustrisTNG might be the reason for the agreement of our prediction of the ICM clumpiness with recent observations beyond the virial radius.

2.6. The gas mass fraction

Finally, we report a first analysis of the gas mass fraction our cluster sample, to explore its validity in terms of the baryon mass budget, and compare it to current observational measurements. The baryonic budget of IllustrisTNG simulations (Nelson et al. 2019) follows the cosmological parameters from the Planck 2015 results (Planck Collaboration et al. 2016).

In our case, we use the average profiles of the ICM density and temperature to estimate the gas mass fraction, under the assumption of hydrostatic equilibrium. Gas mass fractions can be used to probe the hydrostatic mass bias in observations (Wicker et al. 2022). Therefore, we focus here only on the gas cells, and estimate the total mass according to the hydrostatic equilibrium (e.g. Sarazin 1988) within a radius r as

$$M(r) = -\frac{KT(r)r}{\mu m_p G} \left(\frac{d \ln n_e}{d \ln r} + \frac{d \ln T}{d \ln r} \right), \quad (6)$$

where μ is the mean molecular weight of the plasma (see Sect. 4.4 for details), and n_e and T are the electron density and temperature at a give radius r from the center of the clusters. Figure 10 shows the radial profile of the gas mass and of the total mass, for the entire cluster sample. Within the virial radius, the gas mass fraction is in excellent agreement with the ratio of the cosmological parameters Ω_b/Ω_M as measured by the Planck mission (Planck Collaboration et al. 2020), and from various X-ray measurements of the gas mass fraction (e.g. Mantz et al. 2022, 2014; Ettori et al. 2009; Vikhlinin et al. 2006; Lyskova et al. 2023). This agreement is further evidence that the definition of the ICM phase in the IllustrisTNG simulation used in this work does indeed reproduce key features of observed clusters.

For completeness, Fig. 10 includes the radial range beyond r_{200} where it is known that hydrostatic equilibrium is challenged by the presence of non-thermal pressure support (e.g. Fusco-Femiano & Lapi 2018). The application of hydrostatic equilibrium to regions where gas is supported by additional forms of pressure results in a higher-than-true total mass, and in fact our radial profile of the gas mass fraction has a sharp drop. In principle, our analysis can be complemented by a study of the radial distribution of dark matter in IllustrisTNG, which, however, goes beyond the scope of this paper (see Barnes et al. 2021, for details on hydrostatic mass bias for mock X-ray in IllustrisTNG simulation).

3. Projection of the radial profiles

The radial profiles of thermodynamical properties in Fig. 3 up to Fig. 8 are a function of the three-dimensional radius, as measured by the IllustrisTNG simulation. Observations of the thermodynamic quantities, such as density and temperature, and of the associated X-ray surface brightness (see Sect. 4) require either a *deprojection* of the observations (as, e.g., is done in the case of observations such as those of Ghirardini et al. 2019), or a *projection* onto a (focal) plane of the three-dimensional profiles obtained from the simulations. This section described the method of projection that we use for this project, so that we can compare our results with X-ray observations directly, without the need to deproject the observations.

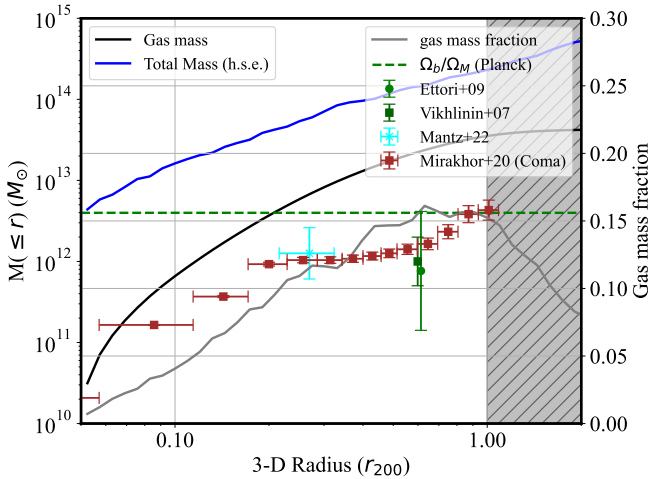


Fig. 10. Cumulative radial profiles of gas mass and hydrostatic mass for the entire cluster sample. The X-ray measurements of Ettori et al. (2009) and Vikhlinin et al. (2006) are for $r \leq r_{500}$, and the Mantz et al. (2022) gas mass fraction was calculated in a radial shell $0.8 - 1.2 \times r_{2500}$, where $r_{2500} \simeq 0.45 \times r_{500}$.

The projection of the radial profiles follows the geometry of Fig. 11, where the spherically-symmetric distribution of matter is represented by onion-like shells of increasing radial distance r from the center. The usual spherical coordinates (r, θ, ϕ) are related to the cylindrical coordinates (ρ, θ, z) by

$$\begin{cases} \rho = r \sin \phi \\ z = r \cos \phi, \end{cases} \quad (7)$$

where the z direction in cylindrical coordinates represents the sightline. Given the spherical symmetry of the radial profiles, the z coordinate of the cylindrical system is chosen to represent the distance along the sightline, and the (ρ, θ) plane represents the focal plane. As illustrated in Fig. 11, the volume of intersection of a spherical shell between radii $R_{\min} = r_{k-1}$ and $R_{\max} = r_k$ and a concentric cylindrical shell between radii ρ_{\min} and ρ_{\max} can be calculated using the following steps.

3.1. The volume of intersection of a sphere with a concentric cylinder

This initial problem consists of finding the volume of intersection of a whole sphere of radius R with a concentric cylinder of radius ρ_{\max} . If $\rho_{\max} \geq R$, the intersection is the entire sphere, so the interesting case is when $\rho_{\max} \leq R$.

The volume element in cylindrical coordinates is $dV = r dr d\theta dz$, and the limits of integration to obtain the volume of intersection are

$$\begin{cases} \rho \in [0, \rho_{\max}] \\ \theta \in [0, 2\pi] \\ z \in [0, z(\rho, R)] \end{cases} \quad (8)$$

where $z(\rho, R)$ represents the maximum value of the Cartesian z coordinate for a fixed value of the ρ cylindrical radius, and it is given by

$$z(\rho, R)^2 + \rho^2 = R^2. \quad (9)$$

Eq. 9 means that, as the cylindrical coordinate spans its range between 0 and ρ_{\max} , the maximum value of z for integration decreases from the sphere's radius R at the center ($\rho = 0$), to a smaller value $z(\rho_{\max}, R) = \sqrt{R^2 - \rho_{\max}^2}$, of course in the interesting case of $\rho_{\max} \leq R$.

This leads to a volume of intersection of

$$V(\rho_{\max}, R) = 2 \int_0^{2\pi} d\theta \int_0^{\rho_{\max}} \rho d\rho \int_0^{\sqrt{R^2 - \rho^2}} dz \quad (10)$$

which can be immediately solved with a change of variable $u = R^2 - \rho^2$, $du = -2\rho d\rho$, again assuming $\rho_{\max} \leq R$, whereby

$$\begin{aligned} V(\rho_{\max}, R) &= 4\pi \int_{R^2}^{R^2 - \rho_{\max}^2} \left(-\sqrt{u} \frac{du}{2} \right) = \\ &= \frac{4}{3} \pi u^{3/2} \Big|_{R^2}^{R^2 - \rho_{\max}^2}. \end{aligned} \quad (11)$$

This integral leads to the results that the volume of intersection of a sphere of radius R with a concentric cylinder of radius ρ_{\max} is given by

$$V(\rho_{\max}, R) = \begin{cases} R^3 & \text{if } R \leq \rho_{\max} \\ \frac{4}{3} \pi \times \left(R^3 - (R^2 - \rho_{\max}^2)^{3/2} \right) & \text{if } R \geq \rho_{\max}. \end{cases} \quad (12)$$

This volume is shown as the grey area in Figure 11.

3.2. Volume of intersection of a spherical shell with a concentric cylinder

The next problem is to intersect a spherical shell with radii R_{\min} , R_{\max} , with the same concentric cylinder of radius ρ_{\max} . The volume of intersection represents the volume contribution from the spherical shell to a circular region of radius ρ_{\max} in the plan of the detector.

For this volume, the cylindrical coordinates have the following ranges:

$$\begin{cases} \rho \in [0, \rho_{\max}] \text{ (same as in previous case)} \\ \theta \in [0, 2\pi] \text{ (same as in previous case)} \\ z \in [z(\rho, R_{\min}), z(\rho, R_{\max})] \end{cases} \quad (13)$$

where the new limits for the z coordinate enforce the two radii of the spherical shell. This geometry is represented in Figure 11.

With the limits of integration according to Eq. 13, the volume of intersection is given by

$$V(\rho_{\max}, R_{\min}, R_{\max}) = 4\pi \int_0^{\rho_{\max}} \rho d\rho \int_{\sqrt{R_{\min}^2 - \rho^2}}^{\sqrt{R_{\max}^2 - \rho^2}} dz \quad (14)$$

provided that $\rho_{\max} \leq R_{\min}$, so that the lower limit of integration remains described by Eq. 9. The case of $R_{\min} \leq \rho_{\max} \leq R_{\max}$ (i.e., in Figure 11 the red dashed line would

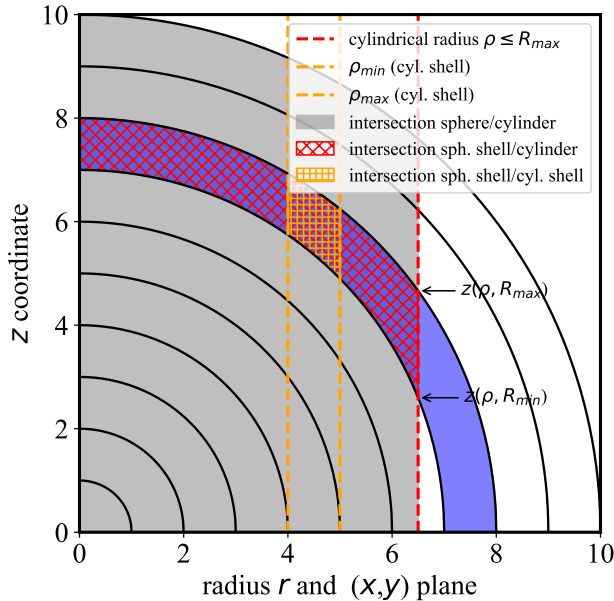


Fig. 11. Volumes of intersection for the projection of a three-dimensional radial distribution onto a two-dimensional plane. In grey is the volume of intersection of concentric sphere and cylinder. In blue is the volume of intersection of a spherical shell with radii R_{\min} , R_{\max} with a cylinder of radius ρ_{\max} (in red). The volume of intersection represents the volume contribution from the spherical shell (assumed to have uniform thermodynamical properties) to a circular region of radius ρ (dashed red line). For a cylindrical shell of radii ρ_{\min} and ρ_{\max} (in orange), the area of intersection represents the contribution to the annulus by the shell. Given the azimuthal symmetry of both sphere and cylinder, the polar angle θ is not displayed.

be between the values $r = 7$ and 8) is not used in practice, and it will be discussed separately. This integral is given by

$$V(\rho_{\max}, R_{\min}, R_{\max}) = \begin{cases} \frac{4}{3}\pi (R_{\max}^3 - R_{\min}^3) & \text{if } \rho_{\max} \geq R_{\max} \\ V(\rho_{\max}, R_{\max}) - V(\rho_{\max}, R_{\min}) & \text{if } \rho_{\max} \leq R_{\min} \\ \text{(unused)} & \text{if } R_{\min} \leq \rho_{\max} \leq R_{\max} \end{cases} \quad (15)$$

In Eq. 15, the top case corresponds to a spherical shell that is completely enclosed by the cylinder. The middle case corresponds to the situation illustrated in Figure 11, where Eq. 14 applies, and therefore the integral is the difference of the two contributions given by Eq. 12 (which has the limitation $\rho_{\max} \leq R_{\min}$). The last case is not used, since we chose the boundaries of the annuli to be the same as those of the spherical shells.

3.3. Volume of intersection of a spherical shell with a concentric cylindrical shell

Finally, the volume of interest is the intersection of a spherical shell with a concentric cylindrical shell of radii ρ_{\min} , ρ_{\max} , and it is represented by the orange shaded area in

Figure 11. To simplify calculations, we chose the same radial bins for the three-dimensional radius r and for the projected cylindrical radius ρ , in such a way that the radii ρ_{\min} , ρ_{\max} always fall at the boundaries of the R_{\min} , R_{\max} spherical radii (i.e., as for the orange dashed lines in Figure 11, but not the red line, which was used only for illustration purposes). With this choice, it is also not necessary to evaluate the case at the bottom of Eq. 15.

Given the linearity of the integral, the volume of intersection is given by

$$V(\rho_{\min}, \rho_{\max}, R_{\min}, R_{\max}) = V(\rho_{\max}, R_{\min}, R_{\max}) - V(\rho_{\min}, R_{\min}, R_{\max}) \quad (16)$$

as the difference of the two contributions according to Eq. 15. This volume is used to integrate the total power or luminosity emitted by a given radial region along the sightline, given that the radiation is expected to be optically thin and therefore the surface brightness adds linearly along the sightline. The use of these equations is explained in the following section.

4. X-ray emission from IllustrisTNG circum-cluster environments: Methods and preliminary results

In this section we present the methods used to calculate and project the X-ray emissivity from the simulated clusters, and preliminary results of our analysis.

4.1. X-ray cooling function, surface brightness and luminosity

In X-ray astronomy, it is customary to refer to the power P emitted by an astrophysical plasma, in units of ergs s^{-1} , as the luminosity of the source. This luminosity is related to the plasma *emissivity* $\Lambda(T, A)$ or *cooling function*, which is defined as the power emitted per unit $n_e n_H$ by the plasma, following the convention of Raymond & Smith (1977) and Smith et al. (2001), and therefore in units of $\text{ergs cm}^3 \text{s}^{-1}$. The plasma emissivity is therefore the power emitted by a unit volume of the plasma, rescaled by the $n_e n_H$, and it is a function of the temperature T and metal composition of the plasma, the latter usually described as a fraction A of Solar abundances of heavy elements. Both the IllustrisTNG simulations and the APEC code of Smith et al. (2001) use the Anders & Grevesse (1989) abundances, and therefore those metal abundances are used in this paper.¹

The plasma cooling function is related to the X-ray surface brightness via

$$S_X = \int_l n_e n_H \Lambda(T, A) dl \quad (\text{erg cm}^{-2} \text{s}^{-1}) \quad (17)$$

where the integral is along the sightline l , and it is intended to represent the amount of energy collected, per unit time, in a unit area of an ideal detector in the focal plane of a focusing telescope. This is the quantity that is usually collected in X-ray observations of diffuse sources such as galaxy clusters (e.g. Ghirardini et al. 2019). Another observational quantity commonly used is the *emission integral*,

¹ The X-ray emissivity is calculated using the ATOMDB and APEC databases, as implemented in the pyatomdb software.

sometimes referred to as *emission measure*, defined by

$$I = \int_V n_e n_H dV \quad (\text{cm}^{-3}) \quad (18)$$

and representing an integral over a volume V of an extended source. The emission integral is proportional to the normalization constant of an optically-thin plasma, such as APEC, used to fit a spectrum from a spatially-resolved area in the detector (e.g., a radial annulus around the center of the cluster), with V representing the three-dimensional volume responsible for the emission. For example, the APEC code (and other commonly used codes such as `mekal`, Mewe et al. 1985, 1986; Kaastra 1992) as implemented in the X-ray fitting software XSPEC returns a normalization constant

$$\text{Norm} = \frac{10^{-14}}{4\pi(D_A(1+z))^2} \times I \quad (19)$$

where D_A is the angular diameter distance to the source, z its redshift, and the constant 10^{-14} is used for convenience so that the normalization constant has values in the neighborhood of unity for a variety of astronomical sources of interest, including galaxy clusters.

For the purpose of comparing the amount of energy radiated by different phases, and at different projected radial distance from the center of the cluster, it is necessary to use quantities that are closely related to observations. We assume radial symmetry throughout this work, and therefore consider the three-dimensional radius r as the only geometric parameter, with R_k a radial range between three-dimensional radii r_{k-1} and r_k , as used in Sect. 2.3. The total power radiated within a *projected* radial range C_k (i.e., projected radii ρ_{k-1} and ρ_k), is thus an integral along the sightline representing a cylindrical shell within those projected radii,

$$P_k = \int_{C_k} \Lambda(T(r), A(r)) \cdot n_e(r) \cdot n_H(r) \cdot dV \quad (\text{erg s}^{-1}) \quad (20)$$

where the volume V is the intersection between the sphere and the concentric cylindrical annulus. In practice, given that three-dimensional radial profiles are evaluated in discrete concentric shells, the power can be evaluated as a sum over all volumes resulting from the intersection of the cylindrical shell (representing the sightline) with the spherical shells (representing the cluster), i.e.,

$$P_k \simeq \sum_{i=1}^N \Lambda_i \cdot n_{e,i} \cdot n_{H,i} \cdot V_{ik} \quad (\text{erg s}^{-1}) \quad (21)$$

where V_{ik} is the volume of intersection of cylindrical shell with radii in the fixed C_k range with a spherical shell with radii in the variable R_i range, as described in Sect. 3, Eq. 16. This projected power is proportional to the *count rate* of photons that are detected by a given instrument, and in a given band, and therefore is a useful proxy to establish the relative level of emission of the phases as a function of projected radius.

In Eq. 21, V_{ik} is the volume of the intersection between the i -th spherical shell of density $n_{e,i}$, and a cylindrical shell with inner and outer radii representing the k -th annulus on the focal plane, the latter were chosen for convenience as the same as those of the k -th spherical shell. Details of

these volumes of intersection were given in Sect. 3, with V_{ik} obtained from Eq. 16 with the two cylindrical radii correspond to the index k , and the two spherical radii to the index i . Given that the radial profiles are given as a function of r/r_{200} , the volume in Eq. 21 must be multiplied by the value of r_{200}^3 in cm^3 to obtain the luminosity in cgs units.

4.2. The PyAtomDB code

This project makes use of the AtomDB data and models of X-ray and extreme ultraviolet emitting astrophysical spectra for hot and optically thin plasma. These data were originally developed by Smith et al. (2001) as the Astrophysical Plasma Emission Database (APED) and the Astrophysical Plasma Emission Code (APEC). These codes result from a development started with Raymond & Smith (1977) and was followed by the codes of Mewe et al. (1985, 1986) and Kaastra (1992). Over the years, as new and improved calculations in atomic data became available, AtomDB was improved by Foster et al. (2012) and eventually led to the PyAtomDB project that is easily accessible through python (Foster & Heuer 2020). The latter is the version that we use in this project.

The AtomDB code provides the emissivity of a plasma in collisional ionization equilibrium (CIE, e.g., Mazzotta et al. 1998), using the Anders & Grevesse (1989) Solar abundances that can be re-scaled, either individually or as a whole, by an overall metal abundance A as a fraction of Solar. Moreover, the emissivity can be conveniently decomposed into the contribution from each element; and, for each element, it is possible to calculate the contribution from each transition, e.g., it is possible to calculate the power of the O VII resonance line at 21.602 Å, or that of any other X-ray line of interest.

4.3. Mean atomic weights of the plasma

Given that the emissivity calculated via atomDB is rescaled by the product ($n_e \cdot n_H$) of the plasma, which is a function of the metal abundances, it is also necessary to specify the mean weights of the various plasma species. In general, the number density of species j is related to the total mass density of the medium ρ via

$$n_j = \frac{\rho X_j}{m_j} \quad (22)$$

where X_j is the *fraction by mass* of the j -th species (say, H, He, electrons, heavy ions, etc.),

$$X_j = \frac{\rho_j}{\rho},$$

and m_j is the atomic mass of the species ($\sim m_p$ for hydrogen, $\sim 4m_p$ for helium, etc.). The mass density ρ (in a given shell) includes all species that are present in the plasma,

$$\rho = \rho_H + \rho_{He} + \rho_z \simeq n_H m_p + n_{He} (4m_p) + \left(\sum_z n_z \cdot m_z \right). \quad (23)$$

where z labels all metals, defined as elements with atomic number $Z > 2$. It is customary to define the hydrogen mass fraction as X , that of helium as Y , and that of all other

metals combined as Z (not to be confused with the same letter that is also used for the overall metal abundance). It is then true that the sum of the mass fractions is

$$X + Y + Z = 1. \quad (24)$$

According to typical Solar abundance ratios, the number density of He is approximately 10% of that of H. Specifically, $n_{\text{He}} \simeq 0.1 \cdot n_{\text{H}}$ according to [Anders & Grevesse \(1989\)](#), while [Lodders \(2003\)](#) finds a number ratio of $n_{\text{He}} = 0.084 \cdot n_{\text{H}}$. Assuming that $Z = 0$ (negligible contribution from metals to mass), and an 8.4% ratio by number of helium-to-hydrogen, the mass fractions are approximately $X = 0.749$ and $Y = 0.251$.

It is now convenient to define the *mean molecular weights* of a given species via

$$\begin{cases} \mu_e = \frac{\rho}{m_p n_e} \\ \mu_H = \frac{\rho}{m_p n_H} \\ \mu_{\text{He}} = \frac{\rho}{m_p n_{\text{He}}} \\ \mu = \frac{\rho}{n m_p} \end{cases}$$

In particular, the mean molecular or atomic weight μ is the average weight (in units of the proton mass m_p) of a given particle using the density of all particles, $n = n_e + n_H + n_{\text{He}} + n_x$. It therefore follows that

$$\frac{1}{\mu} = \frac{1}{\mu_e} + \frac{1}{\mu_H} + \frac{1}{\mu_{\text{He}}} \left(+ \dots + \frac{1}{\mu_z} + \dots \right) \quad (25)$$

where the other terms can be ignored inasmuch as there is a small fraction of metals. Clearly (24) and (25) are equivalent.

Characteristic values for the mean atomic weights in the ICM, assuming fully ionized plasma with primordial abundances (metal mass fraction $Z = 0$), are $\mu_H = 1.335$, $\mu_e = 1.143$, $\mu_{\text{He}} = 15.94$ and $\mu = 0.593$. This means that 1 electron traces an equivalent mass of 1.143 protons, and 1 hydrogen atom traces approximately the mass of 1.335 protons. When metals are taken into account, their values are slightly larger, while the ratio $\mu_H/\mu_e = n_e/n_H \simeq 1.168$ remains approximately the same. From the *IllustrisTNG* simulations we measure a ratio of approximately $n_e/n_H = 1.16$ for all species, at all radii, which is consistent with these calculations.

Collisional ionization equilibrium (CIE) is believed to apply in the hot ICM, and with good approximation also to the lower density warm-hot phase at $\log T(\text{K}) = 5 - 7$. Utilizing the CIE approximation, it is therefore also possible to predict column densities of any ion of interest along a sightline at any projected radius from the center of the cluster, and for any phase. This gives us the ability to study the detectability of absorption lines from a given atomic species. In this initial study, we focus on four ions that are prominent in CIE at the temperatures of the warm-hot phase, namely O VII, O VIII, Ne IX, and Ne X (e.g. [Mazzotta et al. 1998](#)), and probe both their soft X-ray emission and their column densities. A more detailed analysis on their detectability (through current and upcoming X-ray instruments) will be presented in a following paper. Table 2 provides the atomic data for the lines of interest.

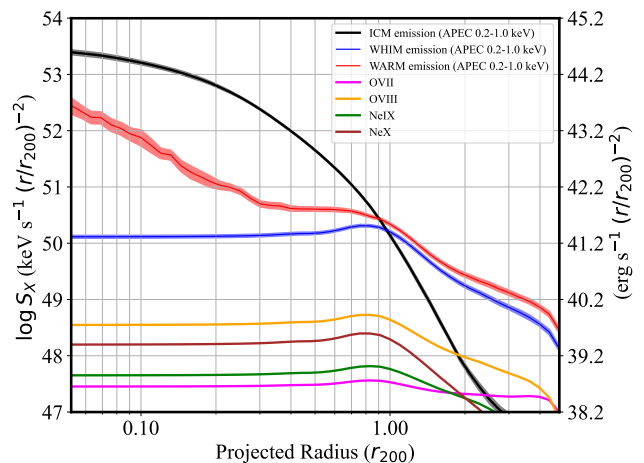


Fig. 12. The X-ray Surface Brightness S_X (Luminosity per unit area) in a soft X-ray band of choice (0.2-1 keV) for the various phases of the gas, for all clusters.

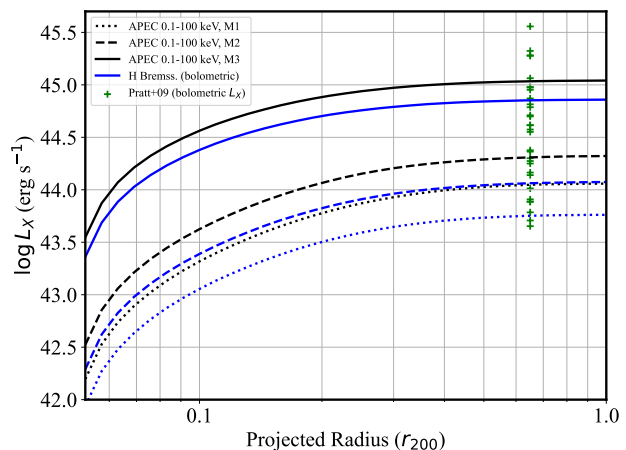


Fig. 13. The X-ray Luminosity in a broad X-ray band (0.1-100 keV) for the ICM phase, for the three cluster mass bins: M_1 (dotted lines), M_2 (dashed lines) and M_3 (solid lines). This broad-band luminosity is compared with bolometric luminosities of massive clusters from [Pratt, G. W. et al. \(2009\)](#)

4.4. The soft X-ray emission near clusters : Initial results

We use Eq. 21 to measure the average luminosity (proportional to the count rate) of the three phases as a function of radial distance from the center of a cluster. Given that the radial profiles are normalized to the r_{200} of each cluster in the *IllustrisTNG* simulations, the volumes $V_{i,k}$ obtained from Eq. 16 are multiplied by r_{200}^3 in units of cm^3 .

Figure 12 features the luminosity per unit area, or surface brightness according to Eq. 17 in a soft X-ray band of choice, as a function of the projected radius, for all the clusters. As illustrated in Figure 12, it is clear that just outside of the virial radius, the luminosity of the warm gas becomes dominant, relative to that of the hot ICM. Inside clusters ($< 1 R_{200}$), the ICM gas dominates the soft X-ray surface brightness. Moreover, the WHIM gas has a very low luminosity inside clusters, while the entire WARM phase has a $\geq 1\%$ surface brightness compared to the hot ICM. As

Ion	Transition	Line Name	Wavelength (Å)	Osc. Strength f	Upper level	Lower level
O VII	$1s^2 - 1s2p$	He α	21.602	0.696	7	1
O VIII	$1s - 2p$	Ly α	18.969 (18.973,18.967)	0.416	3, 4	1
Ne IX	$1s^2 - 1s2p$	He α	13.447	0.724	7	1
Ne X	$1s - 2p$	Ly α	12.134 (12.138,12.132)	0.416	3, 4	1

Table 2. Atomic data for selected X-ray lines of interest, for ions that are expected to be abundant in the warm-hot phase. Upper and lower levels are used for line identification in the APEC database.

discussed previously in section 2, we expect that the soft X-luminosity of warm gas inside clusters is mostly the result of WCGM gas clumps, whereas outside clusters it is mostly induced by WHIM gas. Indeed, beyond $1 R_{200}$, the soft X-ray luminosity of WHIM gas becomes higher than ICM luminosity.

In Fig. 12, we also highlight the contribution of the total emission by selected ions (O VII, O VIII, Ne IX and Ne X), inclusive of their continuum and line emission. Focusing on the metal-line emission, we found that surface brightness of metals is in general decreasing beyond the virial radius, with O VIII the brightest line followed by Ne X, in agreement with previous predictions with OWLS simulations (see Fig. 1 of van de Voort & Schaye 2013). Moreover, our emission of O VII is also consistent with Tuominen et al. (2023) who found that O VII drops dramatically beyond the virial radii of halos in the EAGLE simulations. In detail, beyond the virial radius of massive clusters, the distribution and oxygen ions (primarily O VI and O VII) are expected to follow cosmic filaments (as described in Artale et al. 2022; Tuominen et al. 2023), and thus, oxygen ions might be good tracers of WHIM gas in filaments connected to clusters (Gouin et al. 2022). In fact, Nelson et al. (2018) have used IllustrisTNG simulation to show that O VI, O VII, and O VIII are mostly induced by the WHIM gas phase. Further details on ions abundances and their emissions as a function of their location (e.g., inside or outside filaments) and gas phases will be discussed in detail in another publication.

In order to address the agreement with measurements of the X-ray luminosity from the hot ICM, Fig. 13 shows a bolometric luminosity in a broad X-ray band (0.1-100 keV; black lines) and the bolometric contribution from free-free bremsstrahlung emission from hydrogen alone, for the three cluster mass bins, according to

$$\bar{\epsilon}_{\text{ff}} = 1.4 \times 10^{-27} n_e n_H T^{1/2} \bar{g}_B \text{ (erg s}^{-1} \text{cm}^{-3}) \quad (26)$$

where $\bar{g}_B \simeq 1.2$ is the velocity and frequency-averaged Gaunt factor (e.g., Rybicki & Lightman 1979). In Fig. 13, the bolometric X-ray luminosities from the REXCESS sample of massive clusters out to $r_{500} \simeq 0.65 r_{200}$ are shown as green crosses (Pratt, G. W. et al. 2009). This figure shows that their measurements are consistent with the IllustrisTNG simulated clusters, which spread over a range of cluster masses from 10^{14} to $10^{15} M_{\odot/h}$.

4.5. The soft X-ray emission near clusters due to WARM gas

Figure 14 shows the ratio of WHIM-to-ICM and WARM-to-ICM phases, for the same soft X-ray band as in Fig. 12. This result allows us to highlight the relative importance of the WARM and WHIM gas in the X-ray emission of circum-cluster gas, relative to the usual ICM gas. These

ratios are consistent with an increasing radial trend in the relative count rate from warm sub-virial gas, relative to the virialised ICM, which reaches a ratio of 100% just outside the virial radius. Moreover, the high-density WARM gas is also capable of producing around 10% of soft X-ray excess emission, compared with that from the hot ICM, towards the interior of the cluster. For most massive clusters (M_3 mass bin), in the left panel Fig. 14, the ratio WARM-to-ICM is constant at a value of 10% from radius $0.2r_{200}$ up to $0.7 \times r_{200}$. These results are quantitatively consistent with the presence of soft X-ray excess emission that was detected by ROSAT and other instrument towards Coma out to the virial radius (e.g. Bonamente et al. 2003; Bonamente 2023), and in the inner regions of several other clusters (e.g. Bonamente et al. 2002). An in-depth analysis of the soft excess emission from clusters, which was originally discovered in extreme-ultraviolet observations of Coma and the Virgo clusters (Lieu et al. 1996b,a) will be presented in a follow-up paper.

A comparison of the Bonamente et al. (2022) soft excess emission in Coma with the IllustrisTNG prediction is illustrated in Fig. 15, where only the most massive clusters ($M_{200} > 10^{14.75} M_{\odot/h}$) are used for the prediction, to match Coma's virial mass as measured by Mirakhor & Walker (2020) as $M(r_{200}) = (8.50 \pm 0.55) \times 10^{14} M_{\odot}$. One can see that our numerical prediction of soft X-ray excess via WARM gas emission (red line), is in very good agreement with Coma soft excess (green data points). This emission from warm-hot gas near the virial radius matches the level of soft excess emission detected with ROSAT, indicating a thermal origin for the emission, above the contribution from the hot ICM. Notice that the large scatter of ratio profile, especially from 0.5 to $0.9 r_{200}$, is due to the presence or absence of WARM gas clumps (from one cluster to another), which drastically increase the soft excess, and thus, induce this large scatter traced by the errorbars.

Similar studies were recently performed with the Magneticum simulation (Churazov et al. 2023), finding that the emission from the diffuse WHIM phase alone was not sufficient to explain the observational result of Bonamente et al. (2022). This is also clearly shown by our results when only the WHIM gas is considered (blue curve in Fig. 15). A qualitatively similar result was also obtained by the Cheng et al. (2005) simulations, which identified low-entropy and high-density warm gas as the likely phase responsible for the soft excess within the virial radius.

4.6. Soft X-ray absorption lines : Column density of ions

Our analysis of the IllustrisTNG simulations also measures the column density of any ion of interest, which can be used to address the feasibility of detecting the warm sub-virial gas in absorption. For example, we illustrate in

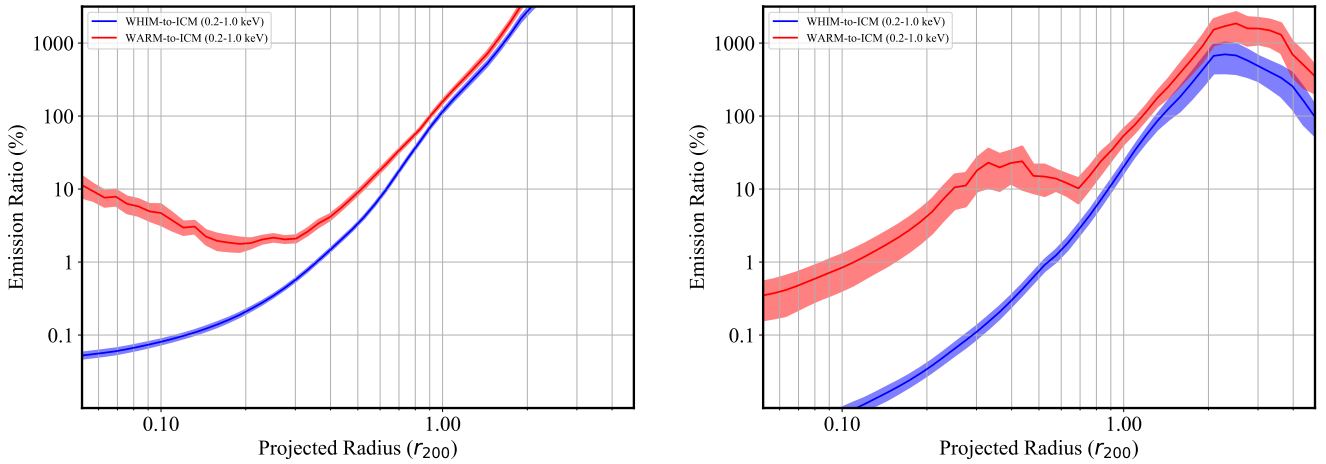


Fig. 14. Ratio of luminosities or count rates of warm phases, relative to the hot ICM, left for all clusters, and right for mass sample M_3 . The figure also shows the contribution of individual ions, primarily through their line emission, to the total emission from warm subvirial phases.

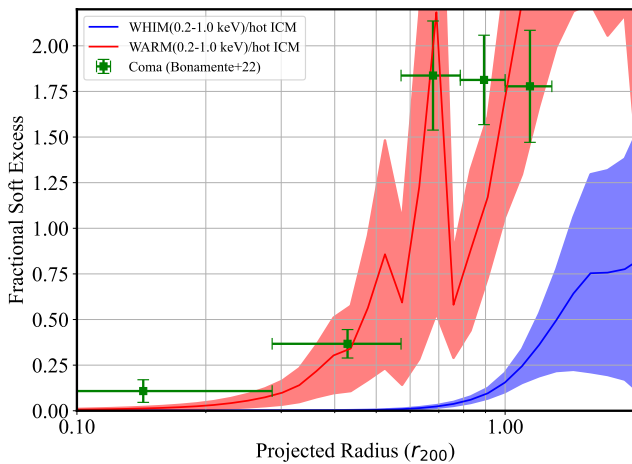


Fig. 15. Ratio of count rates from the warm-hot phases, relative to the hot ICM and same as in Fig. 14, but for the most massive clusters at $M_{200} > 10^{14.75} M_{\odot}/h$ from sample M_4 , to match the mass of the Coma cluster. The data points are the soft excess emission measured by Bonamente et al. (2022) in the 0.2–1.0 keV band, based on the ROSAT analysis of Bonamente et al. (2003).

Fig. 16 the average projected column density of four ions of interest for X-ray absorption studies, viz. O VII, O VIII, Ne IX and Ne X. There have been several reports of possible absorption lines associated from intervening warm-hot gas (recently, e.g., Bonamente et al. 2016; Kovács et al. 2019; Ahoranta et al. 2020, 2021; Spence et al. 2023), although usually with limited significance. In particular, given the lower chance alignment of a bright background extragalactic source (e.g., a quasar) with a galaxy cluster along our sightline, there have been to date no attempts to detect the warm-hot gas in absorption near clusters. Our preliminary results of Fig. 16 indicate that there is especially a substantial amount of O VIII that is in fact within the reach of upcoming X-ray missions such as the proposed *Light Element Mapper (LEM)* mission (Kraft et al. 2022).

These predictions of X-ray absorption lines in circum-cluster environments are done with IllustrisTNG simulation, which already show a good agreement with observations of O VI column density at low redshift (Nelson et al. 2018). Moreover, as recently highlighted by Butler Contreras et al. (2023) using CAMELS simulations, O VII absorption predictions are quite sensitive to change with SN feedback models. Qualitatively, our prediction of O VII column density is in agreement with Butler Contreras et al. (2023) who found that the OVII absorbers with column densities $\log N_{\text{OVII}} < 14 \text{ cm}^{-2}$ fall within 1 Mpc from the center of halos. They thus predicted that the simulated O VII column density are higher in halos and their outskirts than in the large-scale cosmic web. Along this line, the EAGLE simulations analyzed by Wijers & Schaye (2022) estimated the detectability of X-ray metal-line emission from intracluster gas, and found that O VII and O VII emission lines will be detectable out to the virial radius by the proposed Athena X-IFU instrument. These initial results of X-ray absorption lines from the different gas phase in circum-cluster environments illustrate an example of numerical predictions done through our methodology (Sect. 4), and will be explored in more detail a subsequent publication, including the effects of gas clumping and the volume covering fraction.

5. Discussion and conclusions

This paper has presented the methods of analysis for the thermodynamic quantities of simulated galaxy clusters from IllustrisTNG simulation (with $M_{200} > 10^{14} M_{\odot}/h$ at $z = 0$), for the purpose of studying the X-ray emission in the circum-cluster environment. Given the wealth of information provided by these simulations, this paper is intended to be the first in a series of publications where we will analyze the properties of sub-virial gas in and around galaxy clusters, with emphasis on its soft X-ray emission and the effect of the emission on related cluster observables.

Starting from this simulated cluster sample, we extracted azimuthally-averaged radial profiles of the density, temperature and metallicity for different gas phases (e.g. Martizzi et al. 2019b; Galárraga-Espinosa et al. 2021): the

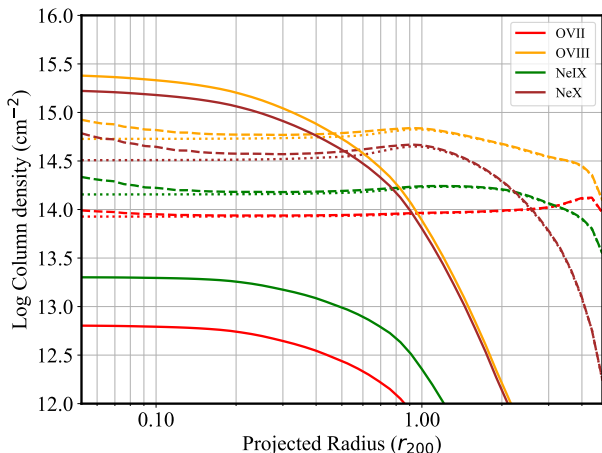


Fig. 16. Projected column densities of selected X-ray ions for all the clusters. Solid curves are for the HOT phase, dashed curves for the WARM and dotted curves for the WHIM phases.

hot ICM phase at $\log T(K) > 7$ and the WARM phase at $5 \leq \log T(K) \leq 7$. The latter was further divided into WHIM ($\log n_H(\text{cm}^{-3}) \leq -4$) and WCGM gas, having higher densities. The goal was to provide a simple yet accurate set of averaged quantities that are representative of the hot virialized gas and of the cooler sub-virial gas that is preferentially found in either filamentary structures (WHIM), or in higher-density regions such as the surroundings of haloes (WCGM). Indeed, based on this same simulated cluster sample, [Gouin et al. \(2022\)](#) have found that gas in the circum-cluster environment is at the interface between the warm gas infalling in filaments connected to clusters, and the hot virialized gas inside clusters (see also [Vurm et al. 2023](#)).

A first step in our analysis was to validate the *IllustrisTNG* data with results from observations of galaxy clusters. Temperature profiles of the hot ICM are well studied in X-rays, and the *IllustrisTNG* profiles (see Sect. 2.3 and Fig. 6) are in excellent agreement with the X-ray measurements of a large sample of X-ray clusters of [Ghirardini et al. \(2019\)](#), and with the [Mirakhor & Walker \(2020\)](#) radial profile of the Coma cluster, one of the nearest and most massive clusters. A similar agreement applies to the measurement of the chemical abundance of the ICM (see Fig. 7), especially towards the virial radius where the abundance of the gas reaches approximately a value of 20% Solar. Another key factor for the prediction of X-ray emission is the amount of inhomogeneities in the plasma, since the emissivity is proportional to the square of the plasma density. Accordingly, we have measured the clumpiness parameter (see Sec. 2.5), and, as expected, we found that the inhomogeneities is increasing with the radial distance from clusters ([Nagai & Lau 2011](#); [Roncarelli et al. 2013](#); [Angelinelli et al. 2021](#)). Our clumpiness radial profile is moreover in good agreement with X-COP clusters ([Eckert et al. 2015a](#)), suggesting a good modeling of AGN feedback, a key ingredient for the study of gas inhomogeneities ([Planelles et al. 2017](#)). Interestingly, separating gas in various phases, we show that both the ICM, WARM, and WHIM gas phases have significant different level of inhomogeneities, within and beyond the virial radius (see Fig. 8).

To study the X-ray radiation from the various plasma phases, we devised a simple analytical method to project the radial profiles of the thermodynamical quantities of interest. This projection, in conjunction with the X-ray emissivity codes and databases provided by the *pyatomdb* project (e.g. [Foster & Heuer 2020](#)), makes it possible to predict the X-ray luminosity and surface brightness profiles projected on a detector plane. A key test for the reliability of our *IllustrisTNG* data is the ability to reproduce the X-ray luminosity of the ICM of observed clusters (see Fig. 13), with bolometric luminosities in the range $\log L_X(\text{erg/s}) = 44 - 45$, similar to that of observed clusters (e.g. [Pratt, G. W. et al. 2009](#)).

This paper has also presented initial results for the analysis of the X-ray emission from the warm sub-virial gas. To date, there are no significant observational constraints on soft X-ray emission from circum-cluster sub-virial plasma, due to the challenges associated with the detection of X-rays in emission at those temperatures. The preliminary analysis of Sect. 4 shows a fundamental new result that is the key take-away from this initial paper: the warm sub-virial gas, either in the form of low-density WHIM gas or as higher-density WCGM, features a surface brightness that is at the same level as that from the ICM near the virial radius, and it becomes the dominant source of soft X-ray radiation at larger distances from the center. This is a key new result that had not been previously appreciated, and it will be the basis for a more detailed investigation in an separate publication.

For example, Fig. 14 shows that the average soft X-ray emission from the WARM gas in entire cluster sample reaches 100% of the ICM emission at $r/r_{200} \simeq 0.8 - 1$ (left panel), with a similar result for the most massive clusters alone (right panel). It is therefore clear that ignoring this emission component would lead to biases in the inference of such quantities as cluster masses measured from X-rays. In the inner cluster regions, the relative importance of the soft X-ray emission from warm gas is usually at a lower level of $\sim 1-10\%$. In particular, focusing on the Coma cluster, and its soft X-ray emission ([Bonamente 2023](#)), we found that the most massive *IllustrisTNG* clusters reproduce well Coma's soft X-ray excess (see Fig. 15), supporting our finding that WARM gas is a crucial ingredient to understand soft X-ray emission in circum-cluster environments.

In summary, the preliminary results presented in this paper are qualitatively consistent with a thermal origin for the cluster soft excess emission detected in a number of clusters, such as in Coma ([Bonamente et al. 2003, 2022](#)) and in other clusters ([Bonamente et al. 2002](#)). The emission, which is at the $\sim 10\%$ level in the inner regions and rising in importance towards the virial radius, is naturally explained by the warm-hot subvirial phases seen in these *IllustrisTNG* simulations. A more detailed analysis of the soft X-ray emission is deferred to a follow-up publication, where we also plan to present results as a function of cluster masses and other structural properties, such as the degree of connectivity that is used as a proxy for the possible presence of WHIM filaments ([Gouin et al. 2022](#)), whether such emission is due to the denser WCGM or to lower-density WHIM filaments, and its dependence on cluster properties.

Acknowledgements. This research has been supported by the funding for the ByoPiC project from the European Research Council (ERC) under the European Union's Horizon 2020 research and innovation program grant agreement ERC-2015-AdG 695561 (ByoPiC,

<https://byopic.eu>). CG thanks the very useful comments and discussions with all the members of the ByoPiC team, and in particular N. Aghanim. We thank the IllustrisTNG collaboration for providing free access to the data used in this work. CG is supported by a KIAS Individual Grant (PG085001) at Korea Institute for Advanced Study.

References

- Ahoranta, J., Finoguenov, A., Bonamente, M., et al. 2021, *A&A*, 656, A107
- Ahoranta, J., Nevalainen, J., Wijers, N., et al. 2020, *A&A*, 634, A106
- Allen, S. W., Schmidt, R. W., Ebeling, H., Fabian, A. C., & van Speybroeck, L. 2004, *MNRAS*, 353, 457
- Anders, E. & Grevesse, N. 1989, *Geochim. Cosmochim. Acta*, 53, 197
- Angelinelli, M., Etti, S., Vazza, F., & Jones, T. W. 2021, *A&A*, 653, A171
- Angelinelli, M., Vazza, F., Giocoli, C., et al. 2020, *MNRAS*, 495, 864
- Ansarifard, S., Rasia, E., Biffi, V., et al. 2020, *A&A*, 634, A113
- Artale, M. C., Haider, M., Montero-Dorta, A. D., et al. 2022, *MNRAS*, 510, 399
- Bahcall, J. N. & Sarazin, C. L. 1977, *ApJ*, 213, L99
- Barnes, D. J., Kay, S. T., Bahé, Y. M., et al. 2017, *MNRAS*, 471, 1088
- Barnes, D. J., Vogelsberger, M., Pearce, F. A., et al. 2021, *MNRAS*, 506, 2533
- Biffi, V., Mernier, F., & Medvedev, P. 2018, *Space Sci. Rev.*, 214, 123
- Bonamente, M. 2022, *Statistics and Analysis of Scientific Data* (Springer, Graduate Texts in Physics, Third Edition)
- Bonamente, M. 2023, arXiv e-prints, arXiv:2302.04011
- Bonamente, M., Joy, M. K., LaRoque, S. J., et al. 2006, *ApJ*, 647, 25
- Bonamente, M., Joy, M. K., & Lieu, R. 2003, *ApJ*, 585, 722
- Bonamente, M., Lieu, R., Joy, M. K., & Nevalainen, J. H. 2002, *ApJ*, 576, 688
- Bonamente, M., Mirakhor, M., Lieu, R., & Walker, S. 2022, *MNRAS*, 514, 416
- Bonamente, M., Nevalainen, J., Tilton, E., et al. 2016, *MNRAS*, 457, 4236
- Butler Contreras, A., Lau, E. T., Oppenheimer, B. D., et al. 2023, *MNRAS*, 519, 2251
- Cen, R. & Ostriker, J. P. 1999, *ApJ*, 514, 1
- Cheng, L.-M., Borgani, S., Tozzi, P., et al. 2005, *A&A*, 431, 405
- Churazov, E., Khabibullin, I. I., Dolag, K., Lyskova, N., & Sunyaev, R. A. 2023, *MNRAS*, 523, 1209
- Cui, W., Knebe, A., Yepes, G., et al. 2018, *MNRAS*, 480, 2898
- Danforth, C. W., Keeney, B. A., Tilton, E. M., et al. 2016, *ApJ*, 817, 111
- Davé, R., Cen, R., Ostriker, J. P., et al. 2001, *ApJ*, 552, 473
- Dolag, K., Komatsu, E., & Sunyaev, R. 2016, *MNRAS*, 463, 1797
- Dubois, Y., Peirani, S., Pichon, C., et al. 2016, *MNRAS*, 463, 3948
- Eckert, D., Jauzac, M., Shan, H., et al. 2015a, *Nature*, 528, 105
- Eckert, D., Roncarelli, M., Etti, S., et al. 2015b, *MNRAS*, 447, 2198
- Eckert, D., Vazza, F., Etti, S., et al. 2012, *A&A*, 541, A57
- Etti, S., Morandi, A., Tozzi, P., et al. 2009, *A&A*, 501, 61
- Foster, A. R. & Heuer, K. 2020, *Atoms*, 8, 49
- Foster, A. R., Ji, L., Smith, R. K., & Brickhouse, N. S. 2012, *The Astrophysical Journal*, 756, 128
- Fusco-Femiano, R. & Lapi, A. 2018, *MNRAS*, 475, 1340
- Galárraga-Espinosa, D., Aghanim, N., Langer, M., & Tanimura, H. 2021, *A&A*, 649, A117
- Ghirardini, V., Eckert, D., Etti, S., et al. 2019, *A&A*, 621, A41
- Ghizzardi, S., Molendi, S., van der Burg, R., et al. 2021, *A&A*, 646, A92
- Giacconi, R., Murray, S., Gursky, H., et al. 1972, *ApJ*, 178, 281
- Gianfagna, G., Rasia, E., Cui, W., et al. 2023, *MNRAS*, 518, 4238
- Gouin, C., Gallo, S., & Aghanim, N. 2022, arXiv e-prints, arXiv:2201.00593
- Hirschmann, M., Dolag, K., Saro, A., et al. 2014, *MNRAS*, 442, 2304
- Kaastra, J. 1992, *Internal SRON-Leiden Rep.*, Ver. 2
- Kovács, O. E., Bogdán, Á., Smith, R. K., Kraft, R. P., & Forman, W. R. 2019, *ApJ*, 872, 83
- Kraft, R., Markevitch, M., Kilbourne, C., et al. 2022, *Line Emission Mapper (LEM): Probing the physics of cosmic ecosystems*
- Kravtsov, A. V. 1999, PhD thesis, New Mexico State University
- Kravtsov, A. V., Klypin, A., & Hoffman, Y. 2002, *ApJ*, 571, 563
- Lieu, R., Mittaz, J. P. D., Bowyer, S., et al. 1996a, *Science*, 274, 1335
- Lieu, R., Mittaz, J. P. D., Bowyer, S., et al. 1996b, *ApJ*, 458, L5
- Lodders, K. 2003, *ApJ*, 591, 1220
- Lyskova, N., Churazov, E., Khabibullin, I. I., et al. 2023, arXiv e-prints, arXiv:2305.07080
- Mantz, A. B., Allen, S. W., Morris, R. G., et al. 2014, *MNRAS*, 440, 2077
- Mantz, A. B., Morris, R. G., Allen, S. W., et al. 2022, *MNRAS*, 510, 131
- Martizzi, D., Vogelsberger, M., Artale, M. C., et al. 2019a, *MNRAS*, 486, 3766
- Martizzi, D., Vogelsberger, M., Artale, M. C., et al. 2019b, *MNRAS*, 486, 3766
- Mazzotta, P., Mazzitelli, G., Colafrancesco, S., & Vittorio, N. 1998, *A&AS*, 133, 403
- Mernier, F., de Plaa, J., Kaastra, J. S., et al. 2017, *A&A*, 603, A80
- Mewe, R., Gronenschild, E. H. B. M., & van den Oord, G. H. J. 1985, *A&AS*, 62, 197
- Mewe, R., Lemen, J. R., & van den Oord, G. H. J. 1986, *A&AS*, 65, 511
- Mirakhor, M. S. & Walker, S. A. 2020, *MNRAS*, 497, 3204
- Mirakhor, M. S. & Walker, S. A. 2021, *Monthly Notices of the Royal Astronomical Society*, 506, 139
- Mirakhor, M. S., Walker, S. A., & Runge, J. 2022, *MNRAS*, 509, 1109
- Mitchell, R. J., Culhane, J. L., Davison, P. J. N., & Ives, J. C. 1976, *MNRAS*, 175, 29P
- Morandi, A., Sun, M., Mulchaey, J., Nagai, D., & Bonamente, M. 2017, *Monthly Notices of the Royal Astronomical Society*, 469, 2423
- Nagai, D. & Lau, E. T. 2011, *ApJ*, 731, L10
- Nelson, D., Kauffmann, G., Pillepich, A., et al. 2018, *MNRAS*, 477, 450
- Nelson, D., Springel, V., Pillepich, A., et al. 2019, *Computational Astrophysics and Cosmology*, 6, 2
- Nevalainen, J., David, L., & Guainazzi, M. 2010, *A&A*, 523, A22
- Parimbelli, G., Branchini, E., Viel, M., Villaescusa-Navarro, F., & ZuHone, J. 2022, arXiv e-prints, arXiv:2209.00657
- Pillepich, A., Springel, V., Nelson, D., et al. 2018, *MNRAS*, 473, 4077
- Planck Collaboration, Ade, P. A. R., Aghanim, N., et al. 2016, *A&A*, 594, A13
- Planck Collaboration, Aghanim, N., Akrami, Y., et al. 2020, *A&A*, 641, A6
- Planelles, S., Fabjan, D., Borgani, S., et al. 2017, *MNRAS*, 467, 3827
- Planelles, S., Mimica, P., Quilis, V., & Cuesta-Martínez, C. 2018, *MNRAS*, 476, 4629
- Pop, A.-R., Hernquist, L., Nagai, D., et al. 2022, arXiv e-prints, arXiv:2205.11528
- Pratt, G. W., Croston, J. H., Arnaud, M., & Böhringer, H. 2009, *A&A*, 498, 361
- Ragagnin, A., Dolag, K., Biffi, V., et al. 2017, *Astronomy and Computing*, 20, 52
- Raymond, J. C. & Smith, B. W. 1977, *ApJS*, 35, 419
- Roncarelli, M., Etti, S., Borgani, S., et al. 2013, *MNRAS*, 432, 3030
- Rybicki, G. B. & Lightman, A. P. 1979, *Radiative Processes in Astrophysics* (New York, Wiley-Interscience)
- Sarazin, C. L. 1988, *X-ray emission from clusters of galaxies*, ed. C. L. Sarazin
- Serlemitsos, P. J., Smith, B. W., Boldt, E. A., Holt, S. S., & Swank, J. H. 1977, *ApJ*, 211, L63
- Smith, R. K., Brickhouse, N. S., Liedahl, D. A., & Raymond, J. C. 2001, *ApJ*, 556, L91
- Snowden, S. L., Freyberg, M. J., Plucinsky, P. P., et al. 1995, *ApJ*, 454, 643
- Spence, D., Bonamente, M., Nevalainen, J., et al. 2023, arXiv e-prints, arXiv:2305.01587
- Tanimura, H., Aghanim, N., Douspis, M., & Malavasi, N. 2022, *A&A*, 667, A161
- Tanimura, H., Aghanim, N., Kolodzig, A., Douspis, M., & Malavasi, N. 2020, *A&A*, 643, L2
- Towler, I., Kay, S. T., & Altamura, E. 2023, *MNRAS*, 520, 5845
- Tuominen, T., Nevalainen, J., Heinämäki, P., et al. 2023, *A&A*, 671, A103
- van de Voort, F. & Schaye, J. 2013, *MNRAS*, 430, 2688
- Vikhlinin, A., Kravtsov, A., Forman, W., et al. 2006, *ApJ*, 640, 691
- Vikhlinin, A., Kravtsov, A. V., Burenin, R. A., et al. 2009, *ApJ*, 692, 1060
- Vurm, I., Nevalainen, J., Hong, S. E., et al. 2023, arXiv e-prints, arXiv:2303.03244
- Walker, S., Simionescu, A., Nagai, D., et al. 2019, *Space Sci. Rev.*, 215, 7
- Wan, J. T., Mantz, A. B., Sayers, J., et al. 2021, *MNRAS*, 504, 1062
- Wicker, R., Douspis, M., Salvati, L., & Aghanim, N. 2022, arXiv e-prints, arXiv:2204.12823
- Wijers, N. A. & Schaye, J. 2022, *MNRAS*, 514, 5214
- Yang, H. Y. K. & Reynolds, C. S. 2016, *ApJ*, 818, 181
- Yoon, J. H. & Putman, M. E. 2013, *ApJ*, 772, L29
- Zhuravleva, I., Churazov, E., Kravtsov, A., et al. 2013, *MNRAS*, 428, 3274

Appendix A: Statistical analysis of the radial profiles

The radial profiles of the thermodynamic quantities (Figures 3 through 8) are obtained by averaging the quantity of interest, for each of the 138 clusters at each of the 50 radii. We then obtain a distribution of the quantity, for all clusters that have data at that radius. At a given radius, not all of the clusters have data, and therefore certain data points — such as those at the lowest radii for the electron density of the WARM phase in Fig. 3, bottom-right panel — result from the use of only a small fraction of all the clusters in the sample. When fewer than 3 clusters have data, we chose not to report that quantity.

With the distribution of the value of the quantity for the ≤ 138 that have data at that radius, we can then calculate key statistics such as the mean, median and standard deviation. In Fig. A.1 we show selected distributions to illustrate the method of analysis. For example, typical distributions of the ICM density use all of the 138 clusters as in the top panel of Fig. A.1, while often only a smaller number of clusters have WHIM or WARM particles at small distances from the cluster center. The bottom panel of Fig. A.1 illustrates a typical situation with the distribution of the clumpiness factor C for the WARM and WHIM phases, whereas the distribution is significantly skewed, resulting in a large difference between the mean and the median. Radial profiles of the ratio of the mean to the median of the distributions, for the ICM and WARM n_H density and for the clumpiness factor, are shown in Fig. A.2, to illustrate the difference between the two statistics. We choose to report the median as the most representative value of the distribution, and its standard deviation as obtained from a Monte Carlo bootstrap resampling method, as a measure of the variability in the distribution.

The choice to use the median as a representative value for a parameter is well documented in the statistical literature, because of its greater insensitivity to outliers, compared to the sample mean (for a review, see, e.g. Bonamente 2022). In fact, most studies of the clumpiness of the gas use the median as a representative value (e.g. Planelles et al. 2017; Nagai & Lau 2011), and similarly for other thermodynamic quantities (e.g. Zhuravleva et al. 2013; Eckert et al. 2015a). Towler et al. (2023) also investigates the difference between the mean and median of certain thermodynamical quantities in simulations (see their Fig. 6), and conclude that mean of density-related quantities are indeed more susceptible to bias due to effect of substructures, compared to the median. In our simulations, we also found this to be true; in fact, in the top panel of Fig. A.2 the datapoint corresponding to $r/r_{200} = 2.75$ is not plotted, as it falls significantly above the scale (for a mean/median ratio above 10,000) due to the effect of a small clump of HOT gas near that radius that is likely unrelated to the hot ICM of one cluster in the sample (cluster number 130).

Appendix B: Tables of radial evolution of cluster properties

This appendix reports the average radial profiles of the thermodynamic properties of gas, namely density and volume covering fraction in Table B.1, temperature and metal abundance in Table B.2, and clumping factor in Table B.3. Each average quantity is reported as a function of phase

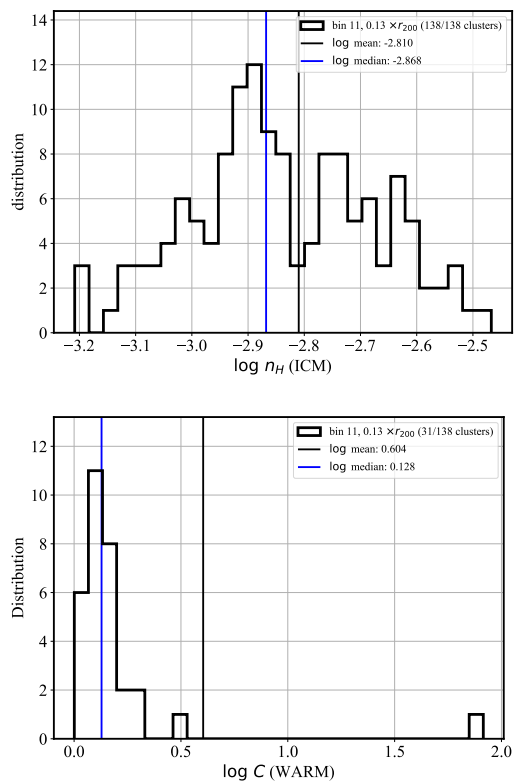


Fig. A.1. Distribution of values of selected quantities from the analysis of the 138 *IllustrisTNG* clusters, for the radial bin 11. Top: ICM density; Bottom: clumpiness factor for WARM phase.

(ICM, WHIM and WARM) and for selected radial distances from the cluster’s center. In each table, the first block is for the median quantity of all the clusters, and the other blocks respectively for the three mass bins in order of increasing average mass (M_1 , M_2 , and M_3).

Table B.1. Density and volume covering fractions of the ICM, WHIM and WARM gas phases in the IllustrisTNG clusters, for representative radii (see Fig. 3 and 4). The four blocks correspond respectively to all clusters followed by mass samples M_1 , M_2 and M_3 .

r/r_{200}	Average n_e Density (cm^{-3}) from (1)			Volume covering fraction f_v from (2)		
	ICM	WHIM	WARM	ICM	WHIM	WARM
0.10	$1.97 \pm 0.08 \times 10^{-3}$...	$9.46 \pm 1.79 \times 10^{-3}$	1.00 ± 0.00	...	$5.59 \pm 1.72 \times 10^{-4}$
0.30	$5.83 \pm 0.07 \times 10^{-4}$...	$1.68 \pm 0.13 \times 10^{-3}$	1.00 ± 0.00	...	$2.04 \pm 0.35 \times 10^{-4}$
0.50	$2.31 \pm 0.02 \times 10^{-4}$	$8.78 \pm 0.13 \times 10^{-5}$	$4.23 \pm 0.18 \times 10^{-4}$	1.00 ± 0.00	$4.58 \pm 2.54 \times 10^{-3}$	$1.47 \pm 0.33 \times 10^{-3}$
0.70	$9.75 \pm 0.07 \times 10^{-5}$	$8.14 \pm 0.12 \times 10^{-5}$	$1.19 \pm 0.03 \times 10^{-4}$	0.97 ± 0.01	$2.23 \pm 0.45 \times 10^{-2}$	$3.29 \pm 0.78 \times 10^{-2}$
1.00	$3.49 \pm 0.07 \times 10^{-5}$	$3.42 \pm 0.06 \times 10^{-5}$	$3.56 \pm 0.10 \times 10^{-5}$	0.69 ± 0.02	0.30 ± 0.02	0.31 ± 0.02
2.00	$2.27 \pm 0.07 \times 10^{-6}$	$3.30 \pm 0.07 \times 10^{-6}$	$3.34 \pm 0.08 \times 10^{-6}$	0.17 ± 0.02	0.83 ± 0.02	0.84 ± 0.02
3.00	$4.63 \pm 0.21 \times 10^{-7}$	$1.49 \pm 0.03 \times 10^{-6}$	$1.52 \pm 0.07 \times 10^{-6}$	0.11 ± 0.01	0.83 ± 0.01	0.82 ± 0.01
4.00	$2.35 \pm 0.29 \times 10^{-7}$	$1.19 \pm 0.03 \times 10^{-6}$	$1.22 \pm 0.04 \times 10^{-6}$	$5.86 \pm 0.69 \times 10^{-2}$	0.63 ± 0.01	0.63 ± 0.01
5.00	$3.83 \pm 0.72 \times 10^{-7}$	$1.22 \pm 0.05 \times 10^{-6}$	$1.24 \pm 0.05 \times 10^{-6}$	$1.67 \pm 0.23 \times 10^{-2}$	0.44 ± 0.01	0.44 ± 0.01
0.10	$1.82 \pm 0.06 \times 10^{-3}$...	$7.68 \pm 0.94 \times 10^{-3}$	1.00 ± 0.00	...	$8.46 \pm 3.87 \times 10^{-4}$
0.30	$5.71 \pm 0.18 \times 10^{-4}$...	$1.51 \pm 0.11 \times 10^{-3}$	1.00 ± 0.00	...	$4.87 \pm 1.85 \times 10^{-4}$
0.50	$2.35 \pm 0.03 \times 10^{-4}$	$9.20 \pm 0.97 \times 10^{-5}$	$3.64 \pm 0.34 \times 10^{-4}$	1.00 ± 0.00	$5.17 \pm 3.06 \times 10^{-3}$	$3.08 \pm 0.43 \times 10^{-3}$
0.70	$9.80 \pm 0.07 \times 10^{-5}$	$8.48 \pm 0.16 \times 10^{-5}$	$1.05 \pm 0.03 \times 10^{-4}$	0.91 ± 0.01	$5.92 \pm 1.37 \times 10^{-2}$	$9.25 \pm 2.66 \times 10^{-2}$
1.00	$3.43 \pm 0.05 \times 10^{-5}$	$3.47 \pm 0.07 \times 10^{-5}$	$3.57 \pm 0.10 \times 10^{-5}$	0.52 ± 0.01	0.47 ± 0.02	0.48 ± 0.02
2.00	$2.19 \pm 0.31 \times 10^{-6}$	$3.16 \pm 0.09 \times 10^{-6}$	$3.20 \pm 0.07 \times 10^{-6}$	$6.30 \pm 1.15 \times 10^{-2}$	0.94 ± 0.01	0.94 ± 0.01
3.00	$4.46 \pm 0.63 \times 10^{-7}$	$1.38 \pm 0.06 \times 10^{-6}$	$1.43 \pm 0.07 \times 10^{-6}$	$4.31 \pm 1.00 \times 10^{-2}$	0.92 ± 0.01	0.92 ± 0.01
4.00	$2.09 \pm 0.27 \times 10^{-7}$	$1.07 \pm 0.06 \times 10^{-6}$	$1.07 \pm 0.05 \times 10^{-6}$	$2.50 \pm 0.68 \times 10^{-2}$	0.72 ± 0.01	0.73 ± 0.01
5.00	$3.08 \pm 0.82 \times 10^{-7}$	$1.06 \pm 0.09 \times 10^{-6}$	$1.08 \pm 0.09 \times 10^{-6}$	$8.78 \pm 3.38 \times 10^{-3}$	0.50 ± 0.01	0.50 ± 0.01
0.10	$1.99 \pm 0.08 \times 10^{-3}$...	$1.37 \pm 0.30 \times 10^{-2}$	1.00 ± 0.00	...	$2.86 \pm 1.12 \times 10^{-4}$
0.30	$5.83 \pm 0.06 \times 10^{-4}$...	$1.78 \pm 0.19 \times 10^{-3}$	1.00 ± 0.00	...	$1.28 \pm 0.36 \times 10^{-4}$
0.50	$2.29 \pm 0.02 \times 10^{-4}$	$8.72 \pm 0.27 \times 10^{-5}$	$4.62 \pm 0.54 \times 10^{-4}$	1.00 ± 0.00	$7.17 \pm 5.82 \times 10^{-3}$	$7.43 \pm 1.82 \times 10^{-4}$
0.70	$9.80 \pm 0.12 \times 10^{-5}$	$7.97 \pm 0.13 \times 10^{-5}$	$1.28 \pm 0.04 \times 10^{-4}$	0.99 ± 0.00	$8.66 \pm 4.01 \times 10^{-3}$	$1.44 \pm 0.36 \times 10^{-2}$
1.00	$3.59 \pm 0.09 \times 10^{-5}$	$3.35 \pm 0.07 \times 10^{-5}$	$3.43 \pm 0.07 \times 10^{-5}$	0.80 ± 0.03	0.21 ± 0.04	0.21 ± 0.04
2.00	$2.40 \pm 0.12 \times 10^{-6}$	$3.36 \pm 0.12 \times 10^{-6}$	$3.41 \pm 0.16 \times 10^{-6}$	0.21 ± 0.01	0.78 ± 0.02	0.79 ± 0.01
3.00	$4.89 \pm 0.35 \times 10^{-7}$	$1.52 \pm 0.08 \times 10^{-6}$	$1.56 \pm 0.08 \times 10^{-6}$	0.16 ± 0.01	0.79 ± 0.02	0.79 ± 0.01
4.00	$3.03 \pm 0.65 \times 10^{-7}$	$1.23 \pm 0.06 \times 10^{-6}$	$1.25 \pm 0.04 \times 10^{-6}$	$7.02 \pm 0.92 \times 10^{-2}$	0.61 ± 0.01	0.61 ± 0.02
5.00	$3.89 \pm 0.50 \times 10^{-7}$	$1.26 \pm 0.05 \times 10^{-6}$	$1.30 \pm 0.04 \times 10^{-6}$	$2.17 \pm 0.63 \times 10^{-2}$	0.42 ± 0.01	0.42 ± 0.01
0.10	$3.41 \pm 0.28 \times 10^{-3}$	1.00 ± 0.00
0.30	$6.35 \pm 0.36 \times 10^{-4}$...	$4.80 \pm 0.54 \times 10^{-3}$	1.00 ± 0.00	...	$1.82 \pm 0.55 \times 10^{-4}$
0.50	$2.32 \pm 0.03 \times 10^{-4}$	$8.24 \pm 0.83 \times 10^{-5}$	$1.63 \pm 0.29 \times 10^{-3}$	1.00 ± 0.00	$7.30 \pm 44.55 \times 10^{-4}$	$3.84 \pm 0.32 \times 10^{-4}$
0.70	$9.10 \pm 0.48 \times 10^{-5}$	$7.45 \pm 0.30 \times 10^{-5}$	$2.31 \pm 0.77 \times 10^{-4}$	1.00 ± 0.00	$1.51 \pm 0.33 \times 10^{-3}$	$9.98 \pm 5.50 \times 10^{-4}$
1.00	$3.16 \pm 0.15 \times 10^{-5}$	$3.68 \pm 0.10 \times 10^{-5}$	$4.95 \pm 0.67 \times 10^{-5}$	0.99 ± 0.00	$1.48 \pm 0.64 \times 10^{-2}$	$1.77 \pm 0.66 \times 10^{-2}$
2.00	$1.87 \pm 0.20 \times 10^{-6}$	$4.11 \pm 0.67 \times 10^{-6}$	$4.23 \pm 0.24 \times 10^{-6}$	0.58 ± 0.01	0.42 ± 0.02	0.42 ± 0.01
3.00	$4.68 \pm 0.21 \times 10^{-7}$	$1.75 \pm 0.08 \times 10^{-6}$	$1.75 \pm 0.24 \times 10^{-6}$	0.37 ± 0.09	0.55 ± 0.02	0.56 ± 0.01
4.00	$2.51 \pm 0.27 \times 10^{-7}$	$1.29 \pm 0.05 \times 10^{-6}$	$1.31 \pm 0.05 \times 10^{-6}$	0.18 ± 0.07	0.45 ± 0.02	0.45 ± 0.02
5.00	$1.18 \pm 0.24 \times 10^{-6}$	$1.49 \pm 0.13 \times 10^{-6}$	$1.56 \pm 0.04 \times 10^{-6}$	$4.80 \pm 2.31 \times 10^{-2}$	0.34 ± 0.01	0.34 ± 0.01

Table B.2. Temperature and chemical abundance of the ICM, WHIM and WARM gas phases in the *IllustrisTNG* clusters, for representative radii (see Fig. 6 and 7). The four blocks correspond respectively to all clusters followed by mass samples M_1 , M_2 and M_3 .

r/r_{200}	Average T (K)			Average metal abundance A (Solar)		
	ICM	WHIM	WARM	ICM	WHIM	WARM
0.10	$3.54 \pm 0.10 \times 10^7$...	$6.52 \pm 0.29 \times 10^6$	0.29 ± 0.01	...	0.68 ± 0.06
0.30	$2.46 \pm 0.05 \times 10^7$...	$8.09 \pm 0.09 \times 10^6$	0.22 ± 0.00	...	0.45 ± 0.01
0.50	$2.06 \pm 0.05 \times 10^7$	$8.74 \pm 0.33 \times 10^6$	$8.44 \pm 0.12 \times 10^6$	0.18 ± 0.00	0.16 ± 0.01	0.30 ± 0.01
0.70	$1.77 \pm 0.07 \times 10^7$	$8.94 \pm 0.06 \times 10^6$	$8.67 \pm 0.03 \times 10^6$	0.14 ± 0.00	0.17 ± 0.00	0.20 ± 0.00
1.00	$1.50 \pm 0.03 \times 10^7$	$7.98 \pm 0.03 \times 10^6$	$7.98 \pm 0.03 \times 10^6$	0.11 ± 0.00	0.14 ± 0.00	0.14 ± 0.00
2.00	$1.35 \pm 0.01 \times 10^7$	$4.99 \pm 0.11 \times 10^6$	$4.99 \pm 0.12 \times 10^6$	$5.13 \pm 0.19 \times 10^{-2}$	$8.30 \pm 0.13 \times 10^{-2}$	$8.31 \pm 0.13 \times 10^{-2}$
3.00	$1.39 \pm 0.03 \times 10^7$	$3.92 \pm 0.05 \times 10^6$	$3.91 \pm 0.06 \times 10^6$	$2.27 \pm 0.19 \times 10^{-2}$	$5.50 \pm 0.17 \times 10^{-2}$	$5.53 \pm 0.18 \times 10^{-2}$
4.00	$1.40 \pm 0.02 \times 10^7$	$2.89 \pm 0.11 \times 10^6$	$2.90 \pm 0.10 \times 10^6$	$9.49 \pm 0.52 \times 10^{-3}$	$4.60 \pm 0.22 \times 10^{-2}$	$4.64 \pm 0.23 \times 10^{-2}$
5.00	$1.34 \pm 0.01 \times 10^7$	$2.19 \pm 0.07 \times 10^6$	$2.20 \pm 0.09 \times 10^6$	$9.76 \pm 0.89 \times 10^{-3}$	$4.95 \pm 0.17 \times 10^{-2}$	$4.91 \pm 0.20 \times 10^{-2}$
0.10	$3.20 \pm 0.03 \times 10^7$...	$6.56 \pm 0.20 \times 10^6$	0.30 ± 0.01	...	0.69 ± 0.06
0.30	$2.09 \pm 0.01 \times 10^7$...	$7.93 \pm 0.36 \times 10^6$	0.24 ± 0.00	...	0.38 ± 0.06
0.50	$1.70 \pm 0.01 \times 10^7$	$9.13 \pm 0.24 \times 10^6$	$8.74 \pm 0.18 \times 10^6$	0.19 ± 0.00	0.16 ± 0.01	0.28 ± 0.01
0.70	$1.46 \pm 0.02 \times 10^7$	$9.07 \pm 0.11 \times 10^6$	$8.88 \pm 0.14 \times 10^6$	0.14 ± 0.00	0.18 ± 0.00	0.20 ± 0.00
1.00	$1.31 \pm 0.02 \times 10^7$	$7.96 \pm 0.03 \times 10^6$	$7.95 \pm 0.02 \times 10^6$	0.10 ± 0.00	0.14 ± 0.01	0.14 ± 0.01
2.00	$1.24 \pm 0.01 \times 10^7$	$4.51 \pm 0.12 \times 10^6$	$4.54 \pm 0.15 \times 10^6$	$4.44 \pm 0.16 \times 10^{-2}$	$8.26 \pm 0.33 \times 10^{-2}$	$8.33 \pm 0.32 \times 10^{-2}$
3.00	$1.25 \pm 0.04 \times 10^7$	$3.62 \pm 0.15 \times 10^6$	$3.62 \pm 0.14 \times 10^6$	$1.88 \pm 0.18 \times 10^{-2}$	$5.59 \pm 0.34 \times 10^{-2}$	$5.53 \pm 0.22 \times 10^{-2}$
4.00	$1.24 \pm 0.02 \times 10^7$	$2.79 \pm 0.15 \times 10^6$	$2.78 \pm 0.14 \times 10^6$	$6.34 \pm 1.05 \times 10^{-3}$	$4.45 \pm 0.30 \times 10^{-2}$	$4.41 \pm 0.30 \times 10^{-2}$
5.00	$1.25 \pm 0.03 \times 10^7$	$1.97 \pm 0.28 \times 10^6$	$2.01 \pm 0.22 \times 10^6$	$7.33 \pm 1.74 \times 10^{-3}$	$4.73 \pm 0.22 \times 10^{-2}$	$4.72 \pm 0.22 \times 10^{-2}$
0.10	$3.74 \pm 0.05 \times 10^7$...	$6.45 \pm 0.81 \times 10^6$	0.29 ± 0.01	...	0.64 ± 0.12
0.30	$2.66 \pm 0.07 \times 10^7$...	$8.10 \pm 0.14 \times 10^6$	0.22 ± 0.00	...	0.47 ± 0.04
0.50	$2.27 \pm 0.09 \times 10^7$	$8.42 \pm 0.49 \times 10^6$	$8.37 \pm 0.14 \times 10^6$	0.17 ± 0.00	0.17 ± 0.02	0.31 ± 0.02
0.70	$1.97 \pm 0.04 \times 10^7$	$8.88 \pm 0.14 \times 10^6$	$8.51 \pm 0.08 \times 10^6$	0.14 ± 0.00	0.17 ± 0.01	0.21 ± 0.01
1.00	$1.62 \pm 0.04 \times 10^7$	$8.16 \pm 0.09 \times 10^6$	$8.14 \pm 0.09 \times 10^6$	0.11 ± 0.00	0.14 ± 0.01	0.14 ± 0.01
2.00	$1.41 \pm 0.03 \times 10^7$	$5.24 \pm 0.16 \times 10^6$	$5.21 \pm 0.16 \times 10^6$	$5.47 \pm 0.28 \times 10^{-2}$	$8.37 \pm 0.16 \times 10^{-2}$	$8.33 \pm 0.12 \times 10^{-2}$
3.00	$1.48 \pm 0.02 \times 10^7$	$4.04 \pm 0.11 \times 10^6$	$4.02 \pm 0.11 \times 10^6$	$2.59 \pm 0.21 \times 10^{-2}$	$5.49 \pm 0.20 \times 10^{-2}$	$5.52 \pm 0.16 \times 10^{-2}$
4.00	$1.45 \pm 0.03 \times 10^7$	$2.99 \pm 0.15 \times 10^6$	$2.98 \pm 0.16 \times 10^6$	$1.05 \pm 0.09 \times 10^{-2}$	$4.70 \pm 0.25 \times 10^{-2}$	$4.75 \pm 0.27 \times 10^{-2}$
5.00	$1.36 \pm 0.01 \times 10^7$	$2.29 \pm 0.11 \times 10^6$	$2.29 \pm 0.11 \times 10^6$	$1.06 \pm 0.08 \times 10^{-2}$	$5.16 \pm 0.42 \times 10^{-2}$	$5.19 \pm 0.43 \times 10^{-2}$
0.10	$6.11 \pm 0.65 \times 10^7$	0.25 ± 0.01
0.30	$4.82 \pm 0.67 \times 10^7$...	$7.02 \pm 0.87 \times 10^6$	0.19 ± 0.00	...	0.90 ± 0.33
0.50	$4.24 \pm 0.07 \times 10^7$	$8.42 \pm 0.26 \times 10^6$	$6.87 \pm 0.29 \times 10^6$	0.16 ± 0.00	0.14 ± 0.04	0.36 ± 0.08
0.70	$3.43 \pm 0.36 \times 10^7$	$8.43 \pm 0.18 \times 10^6$	$7.86 \pm 0.18 \times 10^6$	0.13 ± 0.00	0.14 ± 0.02	0.21 ± 0.05
1.00	$2.58 \pm 0.11 \times 10^7$	$7.66 \pm 0.18 \times 10^6$	$7.54 \pm 0.12 \times 10^6$	0.11 ± 0.00	0.14 ± 0.01	0.14 ± 0.01
2.00	$1.79 \pm 0.10 \times 10^7$	$5.99 \pm 0.06 \times 10^6$	$6.02 \pm 0.05 \times 10^6$	$5.16 \pm 0.47 \times 10^{-2}$	$7.85 \pm 0.65 \times 10^{-2}$	$7.79 \pm 0.31 \times 10^{-2}$
3.00	$1.75 \pm 0.05 \times 10^7$	$4.52 \pm 0.24 \times 10^6$	$4.50 \pm 0.41 \times 10^6$	$2.35 \pm 0.52 \times 10^{-2}$	$5.59 \pm 0.49 \times 10^{-2}$	$5.52 \pm 0.58 \times 10^{-2}$
4.00	$1.87 \pm 0.21 \times 10^7$	$2.96 \pm 0.53 \times 10^6$	$3.05 \pm 0.38 \times 10^6$	$1.32 \pm 0.03 \times 10^{-2}$	$4.86 \pm 0.30 \times 10^{-2}$	$4.81 \pm 0.53 \times 10^{-2}$
5.00	$1.76 \pm 0.05 \times 10^7$	$2.09 \pm 0.45 \times 10^6$	$2.12 \pm 0.45 \times 10^6$	$1.34 \pm 0.35 \times 10^{-2}$	$5.21 \pm 0.88 \times 10^{-2}$	$5.20 \pm 0.87 \times 10^{-2}$

Table B.3. Clumping factor of the ICM, WHIM and WARM gas phases in the IllustrisTNG clusters, for representative radii (see Fig. 8), and for all phases combined. The four blocks correspond respectively to all clusters, followed by mass samples M_1 , M_2 and M_3 .

r/r_{200}	Density clumping factor C from Eq. (5)			
	ICM	WHIM	WARM	All phases
0.10	1.03 ± 0.00	...	1.32 ± 0.07	1.03 ± 0.00
0.30	1.07 ± 0.00	...	1.31 ± 0.04	1.08 ± 0.01
0.50	1.10 ± 0.00	1.03 ± 0.01	1.68 ± 0.09	1.14 ± 0.01
0.70	1.13 ± 0.01	1.05 ± 0.01	1.56 ± 0.10	1.34 ± 0.09
1.00	1.20 ± 0.02	1.21 ± 0.01	1.50 ± 0.06	1.78 ± 0.14
2.00	1.93 ± 0.07	2.91 ± 0.08	4.29 ± 0.25	34.75 ± 4.82
3.00	5.63 ± 1.03	6.75 ± 0.22	11.73 ± 0.66	$2.46 \pm 0.36 \times 10^2$
4.00	13.29 ± 2.08	9.50 ± 0.26	17.00 ± 0.92	$5.41 \pm 0.49 \times 10^2$
5.00	31.29 ± 6.64	10.09 ± 0.26	20.52 ± 1.14	$8.80 \pm 1.02 \times 10^2$
0.10	1.02 ± 0.00	...	1.36 ± 0.07	1.02 ± 0.01
0.30	1.05 ± 0.00	...	1.24 ± 0.13	1.05 ± 0.01
0.50	1.08 ± 0.00	1.03 ± 0.02	1.64 ± 0.16	1.12 ± 0.02
0.70	1.10 ± 0.00	1.04 ± 0.01	1.28 ± 0.05	1.25 ± 0.06
1.00	1.17 ± 0.01	1.17 ± 0.01	1.32 ± 0.04	1.65 ± 0.15
2.00	1.80 ± 0.09	2.74 ± 0.08	3.39 ± 0.35	26.44 ± 9.91
3.00	3.71 ± 0.53	7.05 ± 0.31	11.85 ± 1.01	$3.14 \pm 0.75 \times 10^2$
4.00	9.57 ± 2.81	9.43 ± 0.90	14.66 ± 0.65	$4.54 \pm 1.35 \times 10^2$
5.00	26.99 ± 9.98	10.18 ± 0.63	18.86 ± 4.06	$7.66 \pm 1.70 \times 10^2$
0.10	1.03 ± 0.00	...	1.29 ± 0.02	1.03 ± 0.00
0.30	1.08 ± 0.01	...	1.32 ± 0.03	1.09 ± 0.01
0.50	1.10 ± 0.01	1.03 ± 0.01	1.60 ± 0.05	1.14 ± 0.01
0.70	1.16 ± 0.01	1.06 ± 0.01	1.79 ± 0.11	1.43 ± 0.14
1.00	1.23 ± 0.03	1.22 ± 0.01	1.55 ± 0.05	1.69 ± 0.09
2.00	2.00 ± 0.08	3.07 ± 0.19	4.47 ± 0.29	31.12 ± 5.05
3.00	7.61 ± 1.22	6.71 ± 0.18	10.84 ± 1.03	$1.97 \pm 0.33 \times 10^2$
4.00	15.67 ± 3.78	9.70 ± 0.38	21.01 ± 3.67	$5.77 \pm 1.36 \times 10^2$
5.00	26.90 ± 7.74	10.01 ± 0.27	20.45 ± 0.69	$8.71 \pm 0.99 \times 10^2$
0.10	1.07 ± 0.02	1.07 ± 0.01
0.30	1.10 ± 0.02	...	1.33 ± 0.21	1.11 ± 0.03
0.50	1.16 ± 0.02	1.03 ± 0.01	2.72 ± 0.69	1.25 ± 0.07
0.70	1.23 ± 0.07	1.09 ± 0.03	2.37 ± 0.49	1.55 ± 0.18
1.00	1.24 ± 0.03	1.41 ± 0.03	4.07 ± 0.25	9.10 ± 2.22
2.00	2.14 ± 0.61	3.29 ± 0.11	5.83 ± 0.45	$1.10 \pm 0.41 \times 10^2$
3.00	10.84 ± 2.06	6.29 ± 0.36	16.16 ± 3.43	$6.48 \pm 2.07 \times 10^2$
4.00	37.51 ± 31.92	9.14 ± 0.61	18.98 ± 1.11	$8.34 \pm 2.63 \times 10^2$
5.00	74.81 ± 26.86	10.13 ± 1.13	33.21 ± 7.25	$1.25 \pm 0.36 \times 10^3$

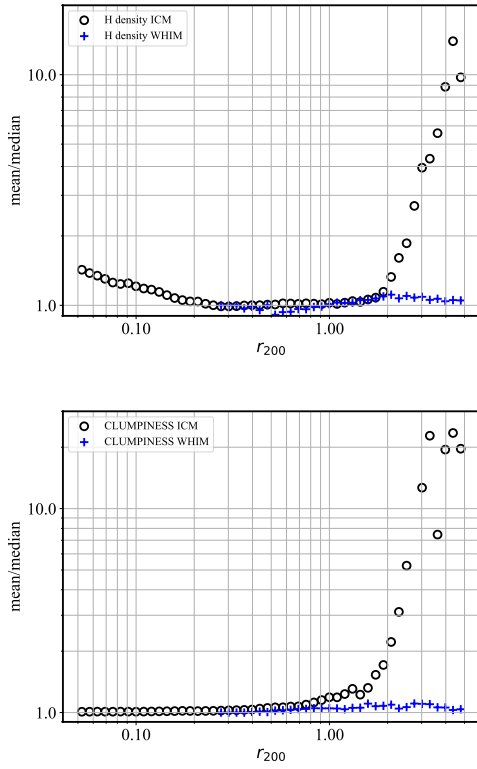


Fig. A.2. Radial distribution of the ratio of the mean to the median for selected quantities. Top: n_H density for the ICM and the WARM gas; Bottom: clumpiness factor.